

# Organic Acid Chemistry in ISM: Detection of Formic Acid and its Prebiotic Chemistry in Hot Core G358.93–0.03 MM1

Arijit Manna<sup>1</sup>, Sabyasachi Pal<sup>1</sup>, Sekhar Sinha<sup>2</sup>, Sushanta Kumar Mondal<sup>2</sup>

<sup>1</sup>Department of Physics and Astronomy, Midnapore City College, Kuturia, Bhadutala, Paschim Medinipur 721129, India

<sup>2</sup>Department of Physics, Sidho-Kanho-Birsha University, Ranchi Road, Purulia 723104, India

Received 20XX Month Day; accepted 2025 Jan 29

**Abstract** In the interstellar medium, formic acid (HCOOH) plays a significant role in the synthesis of the simplest amino acid, glycine ( $\text{NH}_2\text{CH}_2\text{COOH}$ ). The presence of HCOOH suggests that oxygen-bearing molecules may be directly involved in the chemical and physical evolution of star formation regions, particularly in hot molecular cores. This paper presents the first detection of the rotational emission lines of the *trans*-conformer of HCOOH toward the hot molecular core G358.93–0.03 MM1, located in the massive star formation region G358.93–0.03. This study employed high-resolution observations from the Atacama Large Millimeter/submillimeter Array (ALMA) in Band 7. The column density and excitation temperature of *t*-HCOOH are determined as  $(8.13 \pm 0.72) \times 10^{15} \text{ cm}^{-2}$  and  $120 \pm 15 \text{ K}$ , respectively. The fractional abundance of *t*-HCOOH relative to  $\text{H}_2$  is  $(2.62 \pm 0.29) \times 10^{-9}$ . The column density ratios of *t*-HCOOH/ $\text{CH}_3\text{OH}$  and *t*-HCOOH/ $\text{H}_2\text{CO}$  are  $(1.56 \pm 0.12) \times 10^{-2}$  and  $(1.16 \pm 0.12)$ , respectively. We computed a three-phase warm-up chemical model of HCOOH using the gas-grain chemical code UCLCHEM. We found that the observed and modelled abundances of HCOOH are almost identical, within a factor of 0.89. Based on chemical modelling, we showed that HCOOH may be formed through the reaction between HCO and OH on the grain surface, which is further released in the gas-phase.

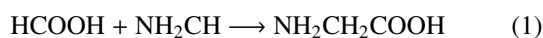
**Key words:** ISM: individual objects (G358.93–0.03) – ISM: abundances – ISM: kinematics and dynamics – stars: formation – astrochemistry

## 1 INTRODUCTION

The number of discoveries of interstellar complex organic molecules (COMs) has increased significantly over the last ten years. In the interstellar medium (ISM) or circumstellar shells, more than 320<sup>1</sup> molecular compounds have been found, including amines ( $\text{R}-\text{NH}_2$ ), carboxamides ( $\text{R}-\text{C}(=\text{O})-\text{NR}_2$ ), alcohols ( $\text{C}_n\text{H}_{2n+1}\text{OH}$ ), acids ( $-\text{COOH}$ ), and aldehydes ( $\text{R}-\text{CH}=\text{O}$ ) (Guélin & Cernicharo 2022). Various types of COMs in ISM represent the essential functional groups needed to initiate the synthesis of ribonucleic acid (RNA) and prebiotic compounds (Redondo et al. 2015; Chaabouni et al. 2020; Herbst & Garrod 2022). Among the detected COMs, various organic acids from different sources have been observed in the gas-phase at low abundances relative to water ( $\text{H}_2\text{O}$ ) (Guélin & Cernicharo 2022). Previous chemical models have indicated that acids play a vital role in the forma-

tion of more complex biomolecules, such as amino acids ( $\text{R}-\text{CH}(\text{NH}_2)-\text{COOH}$ ), in star formation regions, molecular clouds, and planetary atmospheres (Ehrenfreund & Charnley 2000; Garrod & Herbst 2006; Kobayashi et al. 2023).

Among the different types of COMs, formic acid (HCOOH) is one of the most interesting molecules because it is found in ant bites, stinging nettle plants, and bee stings. HCOOH is structurally similar to glycine ( $\text{NH}_2\text{CH}_2\text{COOH}$ ), acetic acid ( $\text{CH}_3\text{COOH}$ ), and methyl formate ( $\text{CH}_3\text{OCHO}$ ). The recent quantum chemical model of Pinto et al. (2025) showed that HCOOH produces  $\text{NH}_2\text{CH}_2\text{COOH}$  in the gas-phase via the following chemical reaction.



In Reaction 1,  $\text{NH}_2\text{CH}$  is one of the isomers of methyleneimine ( $\text{CH}_2\text{NH}$ ), which is formed via the decomposition of  $\text{CH}_2\text{NH}$  under UV radiation (Bouallagui

\* amanna.astro@gmail.com

<sup>1</sup> <https://cdms.astro.uni-koeln.de/classic/molecules>

et al. 2023). Reaction 1 is one of the ideal pathways to the formation of  $\text{NH}_2\text{CH}_2\text{COOH}$  because  $\text{HCOOH}$  and  $\text{CH}_2\text{NH}$  are both found in ISM (Peng et al. 2019; Suzuki et al. 2023; Manna & Pal 2024a). Although  $\text{HCOOH}$  is related to these biologically significant species, it has not received much observational attention. According to the usual astronomical classification,  $\text{HCOOH}$  is not completely a COM because it contains fewer than six atoms (Belloche et al. 2013; Jørgensen et al. 2020; Herbst & Garrod 2022). Since  $\text{HCOOH}$  has an impact on the atmospheric environment, the human body, and the creation of interstellar COMs, it is a particularly significant organic acid (Cao et al. 2014). Quantum chemical studies indicate that  $\text{HCOOH}$  has two conformers, such as *trans* and *cis*, based on the orientation of the single hydrogen bond (Hocking 1976). The three-dimensional molecular structures of the *cis* and *trans* conformers of  $\text{HCOOH}$  are shown in Figure 1, adapted from Järvinen et al. (2018) and reproduced using the molecular modelling software MolView (Bergwerf 2015). Among both conformers, the *trans* conformer of  $\text{HCOOH}$  (hereafter *t*- $\text{HCOOH}$ ) is the most stable, and this conformer was also first found in Sgr B2 with an estimated column density of  $\sim 3 \times 10^{15} \text{ cm}^{-2}$  (Zuckerman et al. 1971). The energy of the ground-vibrational state of *cis*- $\text{HCOOH}$  is  $1365 \pm 30 \text{ cm}^{-1}$ , which is more than that of the *trans* conformer (Hocking 1976). The internal rotation, or the conversion from *trans* to *cis*, has an energy barrier of about  $4827 \text{ cm}^{-1}$  ( $\sim 7000 \text{ K}$ ) (Hocking 1976). In ISM,  $\text{HCOOH}$  was first detected in radio frequencies towards Sgr B2 with an estimated column density of  $\sim 3 \times 10^{15} \text{ cm}^{-2}$  (Zuckerman et al. 1971; Winnewisser & Churchwell 1975). The emission lines of  $\text{HCOOH}$  are also found towards comets (Biver et al. 2014), star-forming regions (Ikeda et al. 2001; Rivilla et al. 2017; Peng et al. 2019), hot molecular cores (Liu et al. 2001, 2002; García de la Concepción et al. 2022), hot corinos (Cazaux et al. 2003; Jørgensen et al. 2018; Ospina-Zamudio et al. 2018), molecular clouds (Zuckerman et al. 1971; Requena-Torres et al. 2006; Rodríguez-Almeida et al. 2021), and cold dark clouds (Irvine et al. 1990; García de la Concepción et al. 2023). The sulphur (S)-bearing counterpart molecules of  $\text{HCOOH}$  are dithioformic acid ( $\text{HC}(\text{S})\text{SH}$ ) and thioformic acid ( $\text{HC}(\text{O})\text{SH}$ ), and both molecules are also detected in ISM (García de la Concepción et al. 2022; Manna & Pal 2023a, 2024b).

It is widely accepted that most stars, including high-mass stars ( $M \geq 8M_\odot$ ), form in extremely dense clusters (Carpenter 2000; Lada & Lada 2003; Rivilla et al. 2013). This theory may also apply to the formation of our Sun (Adams 2010). Investigating the physical and chemical properties of high-mass star-forming regions can provide

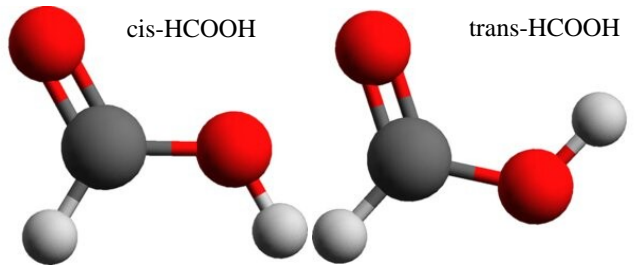


**Fig. 1** Molecular structures of *cis*- $\text{HCOOH}$  and *trans*- $\text{HCOOH}$ . Carbon (C), hydrogen (H), and oxygen (O) atoms are represented by grey, white, and red spheres, respectively.

valuable insight into the early stages of planetary system development. High-mass stars form within the compact ( $D \leq 0.1 \text{ pc}$ ) and dense ( $n \geq 10^5 \text{ cm}^{-3}$ ) cores of interstellar molecular clouds (Kurtz et al. 2000; Beuther et al. 2007; Tan et al. 2014; Yamamoto et al. 2017). As the central high-mass stars evolve slowly, their chemical compositions and physical properties (temperature, density, and luminosity) change (Beuther et al. 2007). Previous observations reveal a sequence of stages, starting with high-mass starless cores (HMSCs), which are dense ( $n \geq 10^5 \text{ cm}^{-3}$ ), cold ( $T \sim 15-20 \text{ K}$ ), and undergo massive molecular condensation without evidence of star formation activity due to gravitational instability (Tan et al. 2013). The next phase is marked by the emergence of high-mass protostellar objects (HMPOs), characterized by protostellar development within hot molecular cores (hereafter HMCs) at temperatures  $T \geq 100 \text{ K}$  and gas densities  $n \geq 10^7 \text{ cm}^{-3}$  (Kurtz et al. 2000; Williams & Viti 2014; Fontani et al. 2007). As the protostar ignites, it emits ultraviolet (UV) photons, ionizes hydrogen, and heats the surrounding medium, thereby creating an  $\text{HII}$  region near the central star (Kurtz et al. 2000). The smaller  $\text{HII}$  regions are associated with younger massive stars, as ionization fronts expand supersonically owing to the stellar radiation pressure (Kurtz et al. 2000). In HMCs, the  $\text{HII}$  regions can be classified based on electron density and size: hypercompact  $\text{HII}$  regions (HC  $\text{HII}$ ) have high densities ( $n \geq 10^6 \text{ cm}^{-3}$ ) and compact sizes ( $R \leq 0.05 \text{ pc}$ ), ultracompact  $\text{HII}$  regions (UC  $\text{HII}$ ) have lower densities ( $n \geq 10^4 \text{ cm}^{-3}$ ) and sizes between  $0.05 \text{ pc}$  and  $0.1 \text{ pc}$ , and classical  $\text{HII}$  regions are larger than  $0.1 \text{ pc}$  (Wood & Churchwell 1989).

The massive star formation region G358.93–0.03 is located at a distance of  $6.75^{+0.37}_{-0.68} \text{ kpc}$ , whose gas mass and luminosity are  $167 \pm 12 M_\odot$  and  $\sim 7.7 \times 10^3 L_\odot$ , respectively (Reid et al. 2014; Brogan et al. 2019). This star formation region has eight dust continuum sources known as G358.93–0.03 MM1 to G358.93–0.03 MM8. Previously, Manna et al. (2023) also found two more strong continuum sources, which are denoted as MM1A and MM2A

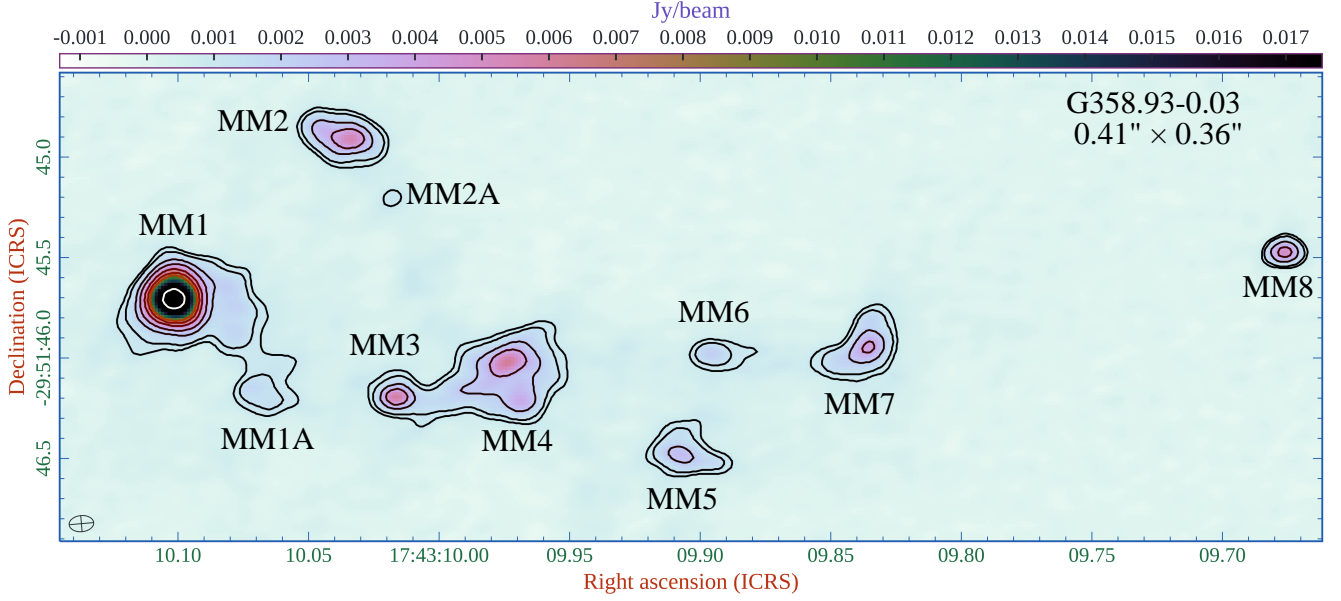


**Fig. 2** The dust continuum emission image of the massive star formation region G358.93–0.03 at a frequency of 291.31 GHz. The synthesized beam size of the continuum image is  $0.41'' \times 0.36''$ . The contour levels increase by a factor of  $\sqrt{2}$  from the starting point of  $2.5\sigma$ .

**Table 1** Dust continuum properties of the detected cores toward G358.93–0.03 at 291.31 GHz.

Source	R.A.	Decl.	Integrated flux (mJy)	Peak flux (mJy beam $^{-1}$ )	RMS (mJy)	Deconvolved source size ('' $\times$ '')	Remark
G358.93–0.03 MM1	17:43:10.1015	-29:51:45.7057	$72.32 \pm 1.82$	$34.61 \pm 0.63$	0.58	$0.48 \times 0.39$	Resolved
G358.93–0.03 MM1A	17:43:10.0671	-29:51:46.4511	$19.62 \pm 3.26$	$5.11 \pm 0.16$	0.23	$0.39 \times 0.34$	Not resolved
G358.93–0.03 MM2	17:43:10.0357	-29:51:44.9019	$22.62 \pm 2.15$	$7.68 \pm 0.62$	0.27	$0.43 \times 0.38$	Resolved
G358.93–0.03 MM2A	17:43:10.0209	-29:51:45.1577	$16.42 \pm 1.49$	$3.47 \pm 0.14$	0.28	$0.42 \times 0.38$	Resolved
G358.93–0.03 MM3	17:43:10.0145	-29:51:46.1933	$62.68 \pm 2.56$	$19.62 \pm 2.63$	0.58	$0.45 \times 0.39$	Resolved
G358.93–0.03 MM4	17:43:09.9738	-29:51:46.0707	$50.75 \pm 2.56$	$12.62 \pm 0.89$	0.65	$0.43 \times 0.37$	Resolved
G358.93–0.03 MM5	17:43:09.9063	-29:51:46.4814	$22.62 \pm 1.35$	$2.45 \pm 0.16$	0.23	$0.44 \times 0.38$	Resolved
G358.93–0.03 MM6	17:43:09.8962	-29:51:45.9802	$12.56 \pm 0.98$	$3.16 \pm 0.16$	0.52	$0.43 \times 0.37$	Resolved
G358.93–0.03 MM7	17:43:09.8365	-29:51:45.9498	$11.26 \pm 0.85$	$2.43 \pm 0.15$	0.62	$0.44 \times 0.38$	Resolved
G358.93–0.03 MM8	17:43:09.6761	-29:51:45.4688	$9.56 \pm 0.62$	$1.48 \pm 0.21$	0.36	$0.40 \times 0.34$	Not resolved

**Table 2** Physical properties of dust continuum sources towards G358.93–0.03.

Source	Mass ( $M_{\odot}$ )	Luminosity ( $L_{\odot}$ )	Dust temperature ( $T_d$ ) (K)	Dust emissivity index ( $\beta$ )	Spectral index <sup>†</sup> ( $\alpha$ )	Density <sup>‡</sup> (cm $^{-3}$ )
G358.93–0.03 MM1	$25.75 \pm 6.36$	$(7.82 \pm 1.23) \times 10^4$	$175 \pm 12$	$1.72 \pm 0.16$	3.72	$1.08 \times 10^8$
G358.93–0.03 MM1A	$11.26 \pm 3.67$	$(4.42 \pm 1.65) \times 10^3$	$35 \pm 4$	$1.56 \pm 0.12$	3.56	$2.36 \times 10^6$
G358.93–0.03 MM2	$13.23 \pm 2.13$	$(8.62 \pm 2.86) \times 10^3$	$42 \pm 5$	$1.62 \pm 0.13$	3.62	$5.25 \times 10^6$
G358.93–0.03 MM2A	$10.12 \pm 4.32$	$(3.16 \pm 1.36) \times 10^3$	$27 \pm 3$	$1.52 \pm 0.18$	3.52	$2.58 \times 10^6$
G358.93–0.03 MM3	$19.21 \pm 4.57$	$(2.98 \pm 1.63) \times 10^4$	$132 \pm 16$	$1.75 \pm 0.25$	3.75	$5.28 \times 10^7$
G358.93–0.03 MM4	$12.58 \pm 3.21$	$(3.56 \pm 1.02) \times 10^3$	$38 \pm 13$	$1.63 \pm 0.15$	3.63	$3.26 \times 10^6$
G358.93–0.03 MM5	$14.47 \pm 2.63$	$(9.65 \pm 2.63) \times 10^3$	$26 \pm 8$	$1.62 \pm 0.16$	3.62	$7.23 \times 10^6$
G358.93–0.03 MM6	$13.03 \pm 1.67$	$(7.23 \pm 1.02) \times 10^3$	$22 \pm 6$	$1.58 \pm 0.23$	3.58	$4.27 \times 10^6$
G358.93–0.03 MM7	$11.53 \pm 2.48$	$(2.22 \pm 1.05) \times 10^3$	$34 \pm 8$	$1.53 \pm 0.22$	3.53	$5.53 \times 10^6$
G358.93–0.03 MM8	$12.62 \pm 3.16$	$(4.63 \pm 1.12) \times 10^3$	$24 \pm 4$	$1.58 \pm 0.27$	3.58	$1.26 \times 10^6$

<sup>†</sup>–The spectral index ( $\alpha$ ) is calculated using the relation  $\alpha = 2 + \beta$  (Beckwith & Sargent 1991).

<sup>‡</sup>–The density ( $n$ ) is estimated using the equation  $n = \frac{N(\text{H}_2)}{2R}$ , where  $R$  is the radius of the core in cm (Liu et al. 2021).

(see Figure 1 in Manna et al. (2023)). In this star formation region, Brogan et al. (2019) classified G358.93–0.03 MM1 and G358.93–0.03 MM3 as hot molecular cores based on the detection of the emission lines of methyl cyanide ( $\text{CH}_3\text{CN}$ ) and maser lines of methanol ( $\text{CH}_3\text{OH}$ ). Recent studies of Manna et al. (2023) and Manna et al. (2024) show that G358.93–0.03 MM1 is a

forest of complex molecules, but G358.93–0.03 MM3 is not molecularly rich. Previously, different chemical compounds were detected towards G358.93–0.03 MM1, such as cyanamide ( $\text{NH}_2\text{CN}$ ) (Manna & Pal 2023b), glycolaldehyde ( $\text{CH}_2\text{OHCHO}$ ) (Manna et al. 2023), ethylene glycol ( $(\text{CH}_2\text{OH})_2$ ) (Manna et al. 2024), formamide ( $\text{NH}_2\text{CHO}$ ) (Manna & Pal 2024c), isocyanic acid (HNCO) (Manna

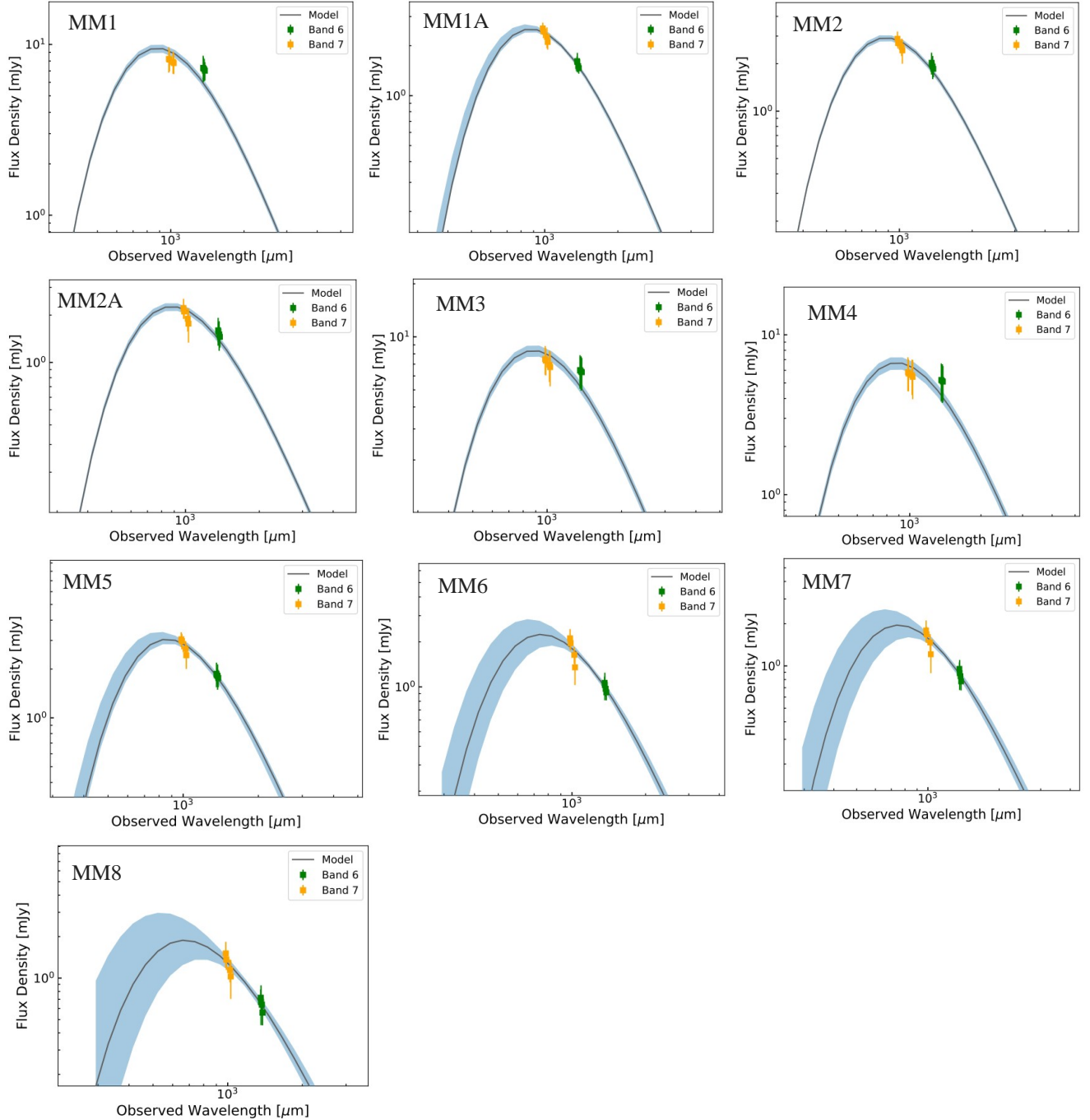


**Fig. 3** SEDs of dust continuum cores from ALMA Band 6 and 7 observations. In the SED plots, orange and green data points represent the observed flux densities of the detected cores across different ALMA bands, with error bars indicating the measurement uncertainties. The black curve corresponds to the best-fit SED obtained using the radiative transfer model by [Robitaille et al. \(2007\)](#), while the blue-shaded region illustrates the  $1\sigma$  uncertainty range of the fit.

& Pal 2024c),  $\text{NH}_2\text{CH}_2\text{COOH}$  precursor molecule methylamine ( $\text{CH}_3\text{NH}_2$ ) (Manna & Pal 2024d), ethylene oxide ( $\text{c-C}_2\text{H}_4\text{O}$ ) (Manna & Pal 2026), and acetaldehyde ( $\text{CH}_3\text{CHO}$ ) (Manna & Pal 2026). After the detection of  $\text{CH}_3\text{NH}_2$ , Manna & Pal (2024d) also searched the emission lines of  $\text{NH}_2\text{CH}_2\text{COOH}$  without any detections. The

upper-limit column densities of  $\text{NH}_2\text{CH}_2\text{COOH}$  conformers I and II are  $\leq 3.26 \times 10^{15} \text{ cm}^{-2}$  and  $\leq 1.20 \times 10^{13} \text{ cm}^{-2}$ , respectively (Manna & Pal 2024d). The identification of different types of molecular compounds indicates that this star formation region is an ideal source for studying various complex biomolecules, including acids.

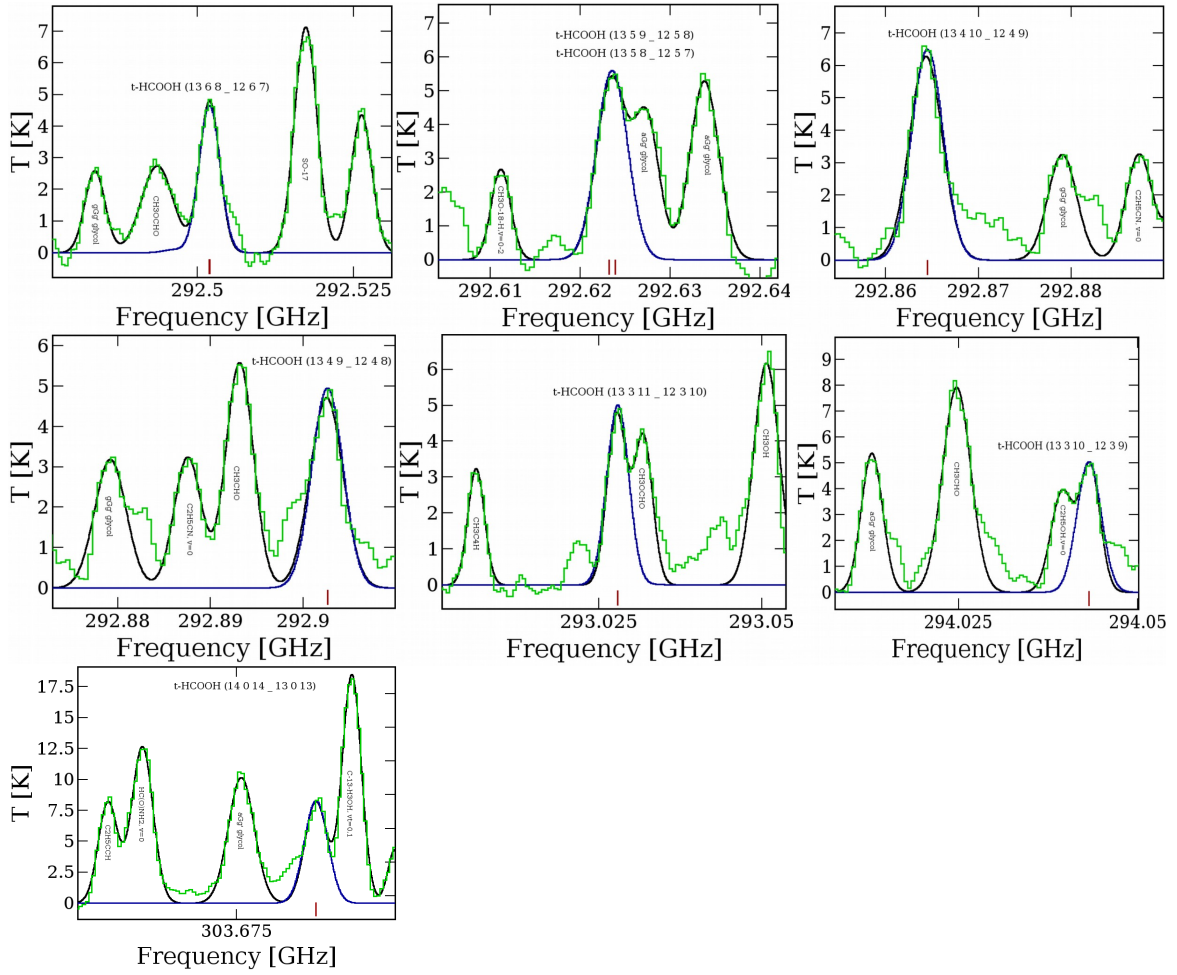


**Fig. 4** Identified molecular emission lines *t*-HCOOH towards G358.93–0.03 MM1. The green lines are the observed spectra, and the blue lines are the LTE spectra of *t*-HCOOH. The black lines are the LTE spectra of the remaining molecules identified in the spectra of G358.93–0.03 MM1.

This paper is presented in the following formats. In section 2, we discuss the ALMA observation and data reduction procedures. The identification of HCOOH and its chemical formation routes are thoroughly described in sections 3 and 4. The summary and conclusion are provided in section 5.

## 2 OBSERVATION AND DATA ANALYSIS

The massive star-forming region G358.93–0.03 was observed using the Atacama Large Millimeter/submillimeter Array (ALMA) Band 7 receivers to study the high-mass protostellar accretion outburst (ID: 2019.1.00768.S, PI: Crystal Brogan). The observations were conducted on October 11th, 2019, with an on-source integration time of 756 seconds. The observed phase centre of G358.93–0.03 was  $(\alpha, \delta)_{J2000} = 17:43:10.000, -29:51:46.000$ . A total of 47 antennas were utilised, providing a minimum baseline of 14 metres and a maximum baseline of 2517 metres.

The calibrator sources used during the observation were J1550+0527 (flux and bandpass calibrator) and J1744–3116 (phase calibrator). The observed frequency ranges for G358.93–0.03 were 290.51–292.39 GHz, 292.49–294.37 GHz, 302.62–304.49 GHz, and 304.14–306.01 GHz, with spectral and velocity resolutions of 1128.91 kHz and 0.96  $\text{km s}^{-1}$ .

Data reduction and imaging were performed using the Common Astronomy Software Application (CASA 5.4.1) in conjunction with the ALMA data analysis pipeline (McMullin et al. 2007; CASA Team et al. 2022). At the time of data analysis, we applied the CASA pipeline tasks SETJY, hifa\_bandpassflag, and hifa\_flagdata for flux calibration, bandpass calibration, and flagging of disruptive antenna data. For flux calibration, the Perley-Butler 2017 flux calibrator model was utilised (Perley & Butler 2017). After the initial data reduction, the target object G358.93–0.03 was split using the MSTRANSFORM task. Using the CASA task TCLEAN with the HOBGOM deconvolver, the

dust continuum images of G358.93–0.03 were produced by utilising line-free channels in the observable frequency ranges. The UVCONTSUB task was used to subtract the background continuum emission from the UV plane of the calibrated data prior to constructing the spectral images. Using the TCLEAN task and the SPEC MODE = CUBE parameter, spectral images of G358.93–0.03 were produced within the observable frequency ranges. To improve the RMS of the final images, we performed three rounds of phase-only self-calibration and one round of amplitude-only self-calibration using the GAINCAL and APPLYCAL tasks. We used the IMPBCOR task to correct the effect of the primary beam pattern in both the spectral and dust continuum images. The final dust continuum and line images were generated using CARTA (Comrie et al. 2021).

### 3 RESULTS

#### 3.1 Dust continuum emission

The dust continuum image of G358.93–0.03 at a frequency of 291.31 GHz is shown in Figure 2. The synthesized beam size and RMS noise level of the image are  $0.41'' \times 0.36''$  and 12.53 mJy, respectively. A total of eight main cores are identified, including two previously known cores associated with G358.93–0.03 MM1 and G358.93–0.03 MM2, hereafter referred to as G358.93–0.03 MM1A and G358.93–0.03 MM2A. To estimate the physical parameters of the detected cores, we performed two-dimensional Gaussian fitting using the task IMFIT. The derived parameters are summarized in Table 1. Most of the dust cores are spatially resolved, except for G358.93–0.03 MM1A and G358.93–0.03 MM8. Previously, Manna et al. (2023) also analyzed this dataset and estimated the H<sub>2</sub> column densities of all cores in G358.93–0.03 based on the dust continuum emission.

##### 3.1.1 Estimation of physical parameters of dust cores

We constructed the spectral energy distribution (SED) of the dust cores in G358.93–0.03 to derive key physical properties, including dust mass, luminosity, dust temperature ( $T_d$ ), and the dust emissivity index ( $\beta$ ). We also estimated the spectral index ( $\alpha$ ) based on the derived values of  $\beta$ . Additionally, we derive the density ( $n$ ) of all cores using the column density of H<sub>2</sub>, with values taken from Manna et al. (2023). The SED incorporates flux density measurements from both ALMA bands 6 and 7, with the band 6 flux values adopted from Manna & Pal (2023b). The observed SEDs were fitted using the radiative transfer models developed by Robitaille et al. (2007). During the fitting procedure, the visual extinction ( $A_v$ ) was constrained to a

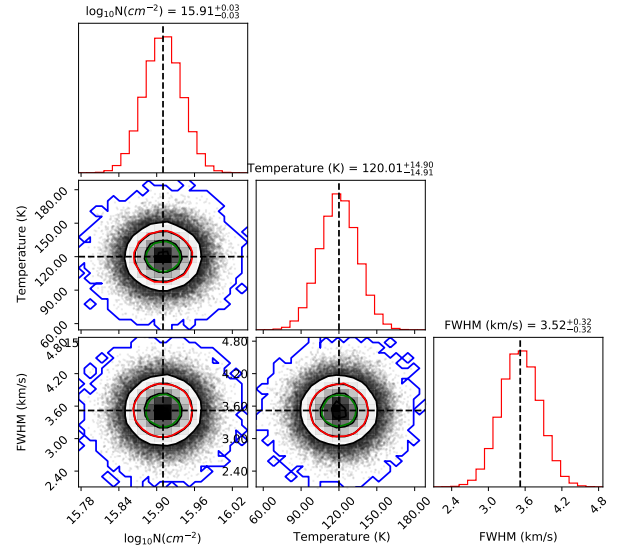


**Fig. 5** Corner plots showing the covariances of the posterior probability distributions of the column density ( $\log_{10}(N)$ ) in  $\text{cm}^{-2}$ , excitation temperature in K, and FWHM in  $\text{km s}^{-1}$  of  $t\text{-HCOOH}$ .

range of 0–30 mag, consistent with the values reported by Furlan et al. (2016), and the source distance was fixed at 6.75 kpc. Details of the radiative transfer fitting methodology can be found in Sanna et al. (2014) and Mininni et al. (2021). The resulting SED fits and the derived dust properties of all cores are presented in Figure 3 and Table 2. We find that the dust temperatures of G358.93–0.03 MM1 and MM3 are higher than those of the other cores, consistent with their identification as HMCs. Previously, Brogan et al. (2019) derived a luminosity of  $7.7 \times 10^3 \text{ L}_\odot$  for G358.93–0.03, but our analysis shows that the hot cores MM1 and MM3 exhibit relatively higher luminosities. We find that the  $\beta$  varies across the cores, ranging from 1.53 to 1.72. These values are consistent with typical ISM dust, where  $\beta \sim 1.6$ , corresponding to maximum grain sizes between approximately 100 Å and 0.3  $\mu\text{m}$  (Weingartner & Draine 2001). We also find that the densities of G358.93–0.03 MM1 and G358.93–0.03 MM3 are  $1.08 \times 10^8$  and  $5.28 \times 10^7 \text{ cm}^{-3}$ , respectively. The other dust cores show relatively lower densities, on the order of  $\sim 10^6 \text{ cm}^{-3}$ . The high densities observed in G358.93–0.03 MM1 and G358.93–0.03 MM3 further support their classification as hot core candidates.

#### 3.2 Line emissions from G358.93–0.03

We found that the hot cores G358.93–0.03 MM1 and G358.93–0.03 MM3 emit molecular line emissions based on the spectral images of G358.93–0.03. We also noticed that the other continuum cores emit no molecular

**Table 3** Spectral line parameters of *t*-HCOOH.

Observed frequency (GHz)	Quantum number	$E_{up}$ (K)	$A_{ij}$ (s $^{-1}$ )	$g_{up}$	$S\mu^2$ <sup>★</sup> (Debye $^2$ )	FWHM (km s $^{-1}$ )	$\int T_{mb} dV$ <sup>†</sup> (K km s $^{-1}$ )	Remark
292.501*	13(6,8)–12(6,7)	212.63	2.23 $\times 10^{-4}$	27	20.67	3.53 $\pm 0.21$	17.31 $\pm 2.52$	Non blended
292.623	13(5,9)–12(5,8)	177.71	2.42 $\times 10^{-4}$	27	22.37	3.51 $\pm 0.41$	16.71 $\pm 3.75$	Non blended
292.623	13(5,8)–12(5,7)	177.71	2.42 $\times 10^{-4}$	27	22.37	3.51 $\pm 0.32$	16.75 $\pm 3.62$	Non blended
292.864	13(4,10)–12(4,9)	149.16	2.57 $\times 10^{-4}$	27	23.77	3.54 $\pm 0.27$	21.92 $\pm 4.28$	Non blended
292.902	13(4,9)–12(4,8)	149.16	2.58 $\times 10^{-4}$	27	23.77	3.51 $\pm 0.36$	15.51 $\pm 2.74$	Non blended
293.027	13(3,11)–12(3,10)	126.96	2.70 $\times 10^{-4}$	27	24.87	3.54 $\pm 0.46$	15.78 $\pm 2.63$	Non blended
294.043	13(3,10)–12(3,9)	127.09	2.73 $\times 10^{-4}$	27	24.86	3.55 $\pm 0.13$	15.14 $\pm 2.43$	Non blended
303.687	14(0,14)–13(0,13)	110.93	3.17 $\times 10^{-4}$	29	28.17	3.52 $\pm 0.19$	24.06 $\pm 4.16$	Non blended

\*—Those transitions of *t*-HCOOH are contained double with frequency difference of  $\leq 100$  kHz. The second transition is not shown.

★—The values of  $S\mu^2$  is taken from the [Splatalogue](#).

†—The values of  $\int T_{mb} dV$  is estimated by fitting the Gaussian model.

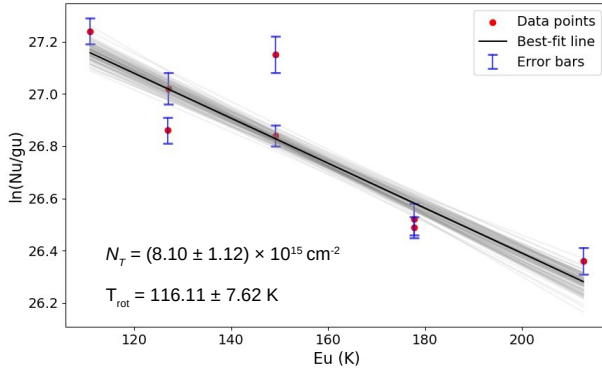


**Fig. 6** Rotational diagram of *t*-HCOOH for the estimation of the total column density ( $N_T$ ) and rotational temperature ( $T_{rot}$ ) of *t*-HCOOH using the MCMC approach. The grey lines are the random draws from the fit posteriors, and the solid black line in the rotational diagram represents the best-fit straight line.

lines. The synthesized beam sizes for the spectral images are  $0.42'' \times 0.37''$ ,  $0.43'' \times 0.37''$ ,  $0.41'' \times 0.37''$ , and  $0.41'' \times 0.36''$  at frequency ranges of 290.51–292.39 GHz, 292.49–294.37 GHz, 302.62–304.49 GHz, and 304.14–306.01 GHz, respectively. We extracted line spectra from G358.93–0.03 MM1 and G358.93–0.03 MM3 using a  $0.52''$  diameter circular region, which encompasses the line-emitting regions of both hot cores. The extracted spectra are shown in Figure 2 of [Manna et al. \(2023\)](#). Based on the molecular spectra, we see that G358.93–0.03 MM1 is more chemically rich than G358.93–0.03 MM3. We observed some emission lines of  $\text{CH}_3\text{OH}$ ,  $\text{H}_2\text{CO}$ , and CS showing the outflow nature. The systematic velocities ( $V_{LSR}$ ) of the molecular spectra of G358.93–0.03 MM1 and G358.93–0.03 MM3 are  $-16.5 \text{ km s}^{-1}$  and  $-18.5 \text{ km s}^{-1}$ , respectively ([Brogan et al. 2019](#)).

Following spectrum extraction, we used the CASSIS software to identify molecules and analyse spectra using the local thermodynamic equilibrium (LTE) model with the help of molecular spectroscopic databases from

the Jet Propulsion Laboratory (JPL) and Cologne Database for Molecular Spectroscopy (CDMS) ([Vastel et al. 2015](#); [Pickett et al. 1998](#); [Müller et al. 2005](#)). We determine the excitation temperatures and column densities of the identified molecules using the LTE-modelled spectra. CASSIS uses the following formula to determine the brightness temperature ( $T_b$ ) of the molecular spectra:

$$T_b = T_C e^{-\tau} + (1 - e^{-\tau})(J_\nu(T_{ex}) - J_\nu(\text{CMB})) \quad (1)$$

In equation 1,  $J_\nu(T) = (h\nu/k) \times 1/(e^{h\nu/kT} - 1)$  is the radiation temperature,  $\tau$  is the optical depth,  $T_C$  is the continuum temperature, and CMB is the cosmic microwave background at 2.7 K. We fitted the LTE-modelled spectra of molecules over the observed spectra using the Markov chain Monte Carlo (MCMC) technique in the CASSIS. The first step of the MCMC method is to choose an initial point ( $X_0$ ) at random from the four-dimensional parameter space. After that, it iteratively creates neighbouring points ( $X_1$ ) using a dynamically modified step size. After evaluating each new point's  $\chi^2$  value, the new point is accepted if the ratio  $p = \chi^2(X_0)/\chi^2(X_1)$  is greater than 1. Even so, the method can avoid local minima and fully search the parameter space if  $p$  is smaller than 1 because the new point may still be accepted with a given probability. In our MCMC study, we used 2000 walkers, evenly distributed throughout defined parameter ranges. For absolute convergence, we ran the chains for 22000 steps. In order to achieve the best fit, this method allows us to simultaneously change all of the parameters, such as column density, excitation temperature, full width at half maximum (FWHM), and  $V_{LSR}$ . CASSIS calculated the partition functions of the identified molecules using the following expression:

$$Q(T) = \sum_i g_i \times \exp(-E_i/kT) \quad (2)$$

In equation 2,  $g_i$  and  $E_i$  represent the statistical weight and energy of the  $i$ th energy level, respectively. We employed a source size of  $\sim 0.5''$  (the half-maximum diameter of our

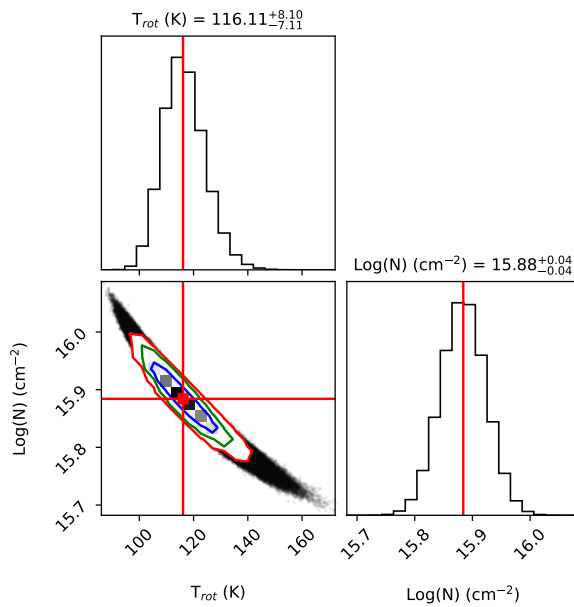


**Fig. 7** Marginalized posterior probability distribution (corner plot) of column density and rotational temperature of *t*-HCOOH using the MCMC approach.

**Table 4** Derived emitting regions of *t*-HCOOH.

Observed frequency (GHz)	Quantum number	$E_u$ (K)	$\theta_s$ (")
292.501	13(6,8)–12(6,7)	212.63	0.41
292.623	13(5,9)–12(5,8)	177.71	0.42
292.623	13(5,8)–12(5,7)	177.71	0.42
292.864	13(4,10)–12(4,9)	149.16	0.40
292.902	13(4,9)–12(4,8)	149.16	0.42
293.027	13(3,11)–12(3,10)	126.96	0.43
294.043	13(3,10)–12(3,9)	127.09	0.42
303.687	14(0,14)–13(0,13)	110.93	0.41

beam size) for LTE spectral modelling. We evaluated the column density, excitation temperature, and FWHM of the detected molecule following spectrum analysis using the LTE models. Additionally, we use the column densities of identified molecules and divide them by the H<sub>2</sub> column density to estimate the fractional abundances of detected molecules. After spectral analysis, we found the rotational emission lines of *t*-HCOOH, which are discussed in the next section.

### 3.2.1 *t*-HCOOH towards G358.93–0.03 MM1

Following spectral analysis, we identified a total of 8 transition lines of *t*-HCOOH towards G358.93–0.03 MM1, where upper-state energies ( $E_{up}$ ) change between 110.93 K and 212.63 K. This is the first time this molecule has been found in G358.93–0.03 MM1, as far as we know. After spectral analysis, we found that all detected emission lines of *t*-HCOOH within the studied frequency ranges

are non-blended and detected above  $3.5\sigma$  significance. We also observed that  $J = 13(5,9)–12(5,8)$  and  $J = 13(5,8)–12(5,7)$  transitions of *t*-HCOOH are found in the single spectral line because those transitions are located in the short frequency span. Figure 4 and Table 3 display the LTE-fitted spectral lines and line parameters of *t*-HCOOH. For *t*-HCOOH, the column density ( $N$ ), excitation temperature ( $T_{ex}$ ), and FWHM are  $(8.13 \pm 0.72) \times 10^{15} \text{ cm}^{-2}$ ,  $120 \pm 15 \text{ K}$ , and  $3.52 \pm 0.32 \text{ km s}^{-1}$ , respectively, based on the posterior probability distribution shown in Figure 5. The fractional abundance of *t*-HCOOH with respect to H<sub>2</sub> is  $(2.62 \pm 0.29) \times 10^{-9}$ , where the column density of H<sub>2</sub> towards G358.93–0.03 MM1 is  $(3.1 \pm 0.2) \times 10^{24} \text{ cm}^{-2}$  (Manna et al. 2023). During spectral analysis, we also detected the emission lines of CH<sub>3</sub>OH and H<sub>2</sub>CO in the spectra of G358.93–0.03 MM1, and we discuss the detailed physical and chemical properties of both molecules in a separate paper. We noticed that emission lines of H<sub>2</sub>CO show an outflow nature. In the case of CH<sub>3</sub>OH, we see the lower  $E_{up}$  ( $\leq 50$  K) of CH<sub>3</sub>OH lines show outflows nature, but higher  $E_{up}$  ( $\geq 70$  K) CH<sub>3</sub>OH lines show compact nature, meaning those lines are emitted from the warm inner region of G358.93–0.03 MM1. To confirm the outflow nature of both CH<sub>3</sub>OH and H<sub>2</sub>CO, we constructed channel maps for each molecule using the transitions  $J = 2(1,0)–2(0,+0)$  for CH<sub>3</sub>OH and  $J = 4(0,4)–3(0,3)$  for H<sub>2</sub>CO. The channel maps, along with the corresponding spectra of CH<sub>3</sub>OH and H<sub>2</sub>CO, are presented in Figures A1 and A2, respectively. The column density and excitation temperature of H<sub>2</sub>CO are  $(7.02 \pm 0.35) \times 10^{15} \text{ cm}^{-2}$  and  $90 \pm 6 \text{ K}$ . The column density and excitation temperature of CH<sub>3</sub>OH, which exhibit the outflow nature, are  $(8.52 \pm 0.46) \times 10^{16} \text{ cm}^{-2}$  and  $80 \pm 7 \text{ K}$ . The column density and excitation temperature of CH<sub>3</sub>OH, which emitted from the warm inner region, are  $(5.21 \pm 0.22) \times 10^{17} \text{ cm}^{-2}$  and  $152 \pm 16 \text{ K}$ . The column density ratios of *t*-HCOOH/CH<sub>3</sub>OH and *t*-HCOOH/H<sub>2</sub>CO are  $(1.56 \pm 0.12) \times 10^{-2}$  and  $(1.16 \pm 0.12)$ . To estimate the *t*-HCOOH/CH<sub>3</sub>OH value, we use the column density of CH<sub>3</sub>OH, which is emitted from the warm inner regions. After the detection of *t*-HCOOH, we also searched for the emission lines of *c*-HCOOH, but we observed that all detected lines of *c*-HCOOH are blended. So, we estimated the upper-limit column density of *c*-HCOOH to be  $\leq (7.25 \pm 0.83) \times 10^{14} \text{ cm}^{-2}$ .

### 3.2.2 Estimation of rotational temperature: Rotational diagram

We have computed a rotational diagram based on the eight non-contaminated transitions of *t*-HCOOH in order to determine the rotational temperature ( $T_{rot}$ ) and total column density ( $N_T$ ). The rotational diagram is essential for con-

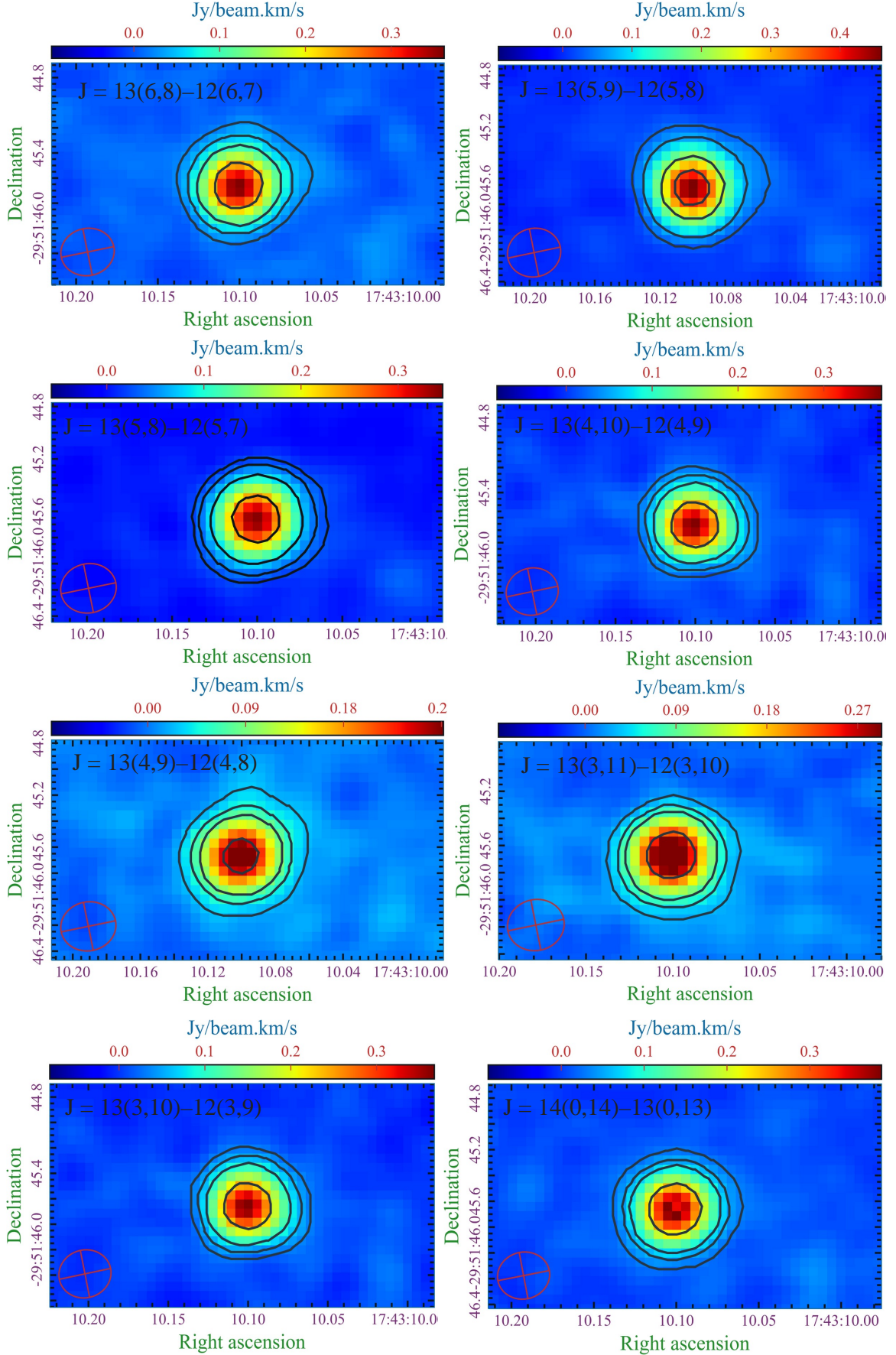


**Fig. 8** Integrated intensity images (moment zero maps) of the detected transitions of *t*-HCOOH towards G358.93–0.03 MM1. The black contours are the 291.31 GHz continuum emission, and the contour levels are at 20%, 40%, 60%, and 80% of the peak flux. The red circles represent the synthesized beam of the intensity images.

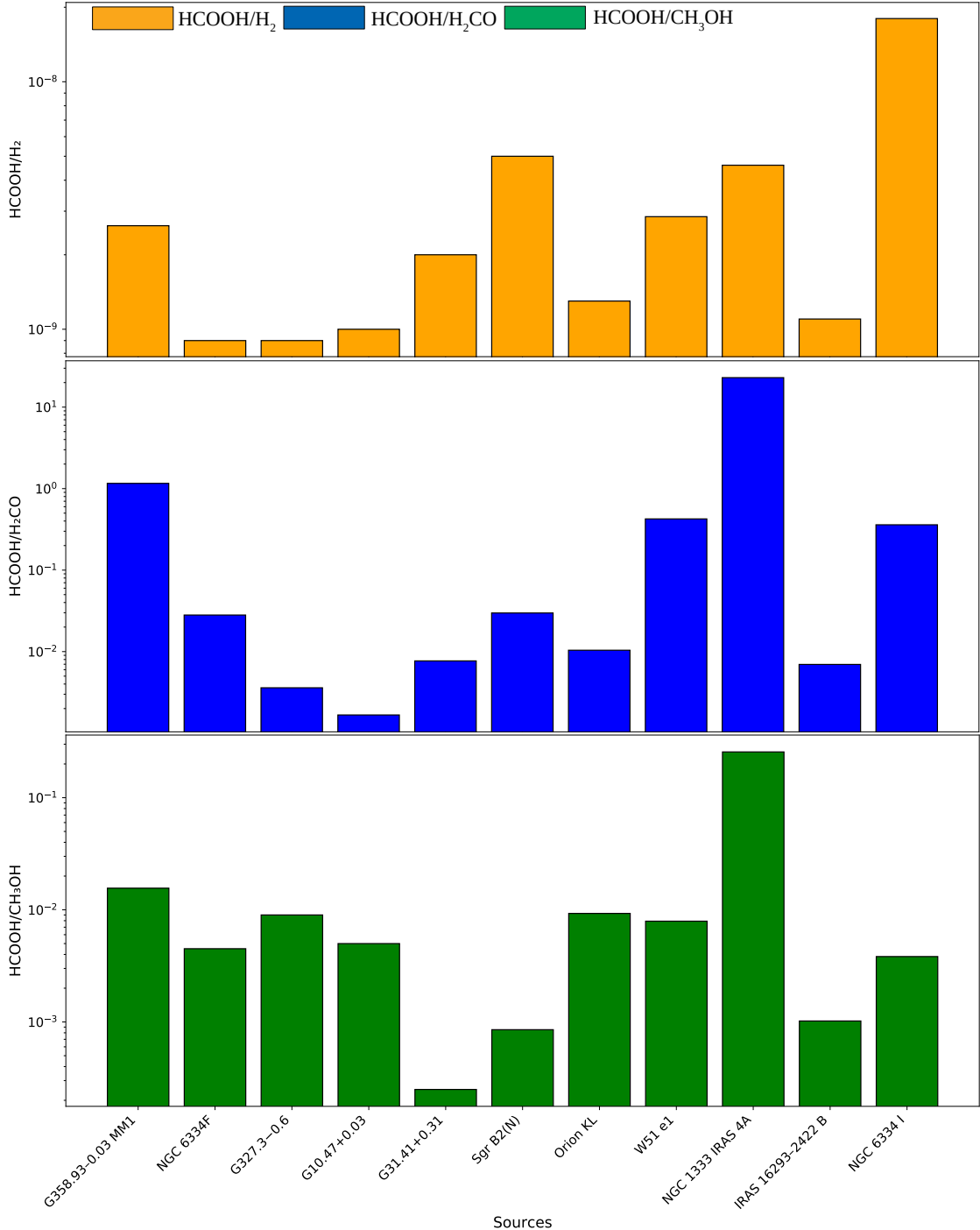


**Fig. 9** Comparison of the abundances of HCOOH relative to H<sub>2</sub> (upper panel), H<sub>2</sub>CO (middle panel), and CH<sub>3</sub>OH (lower panel) towards G358.93–0.03 MM1, with different hot cores (i.e., NGC 6334F, G327.3–0.6, G10.47+0.03, G31.41+0.31, Sgr B2(N), Orion KL, W51 e1, NGC 6334 I), and hot corinos (i.e., NGC 1333 IRAS 4A, IRAS 16293–2422 B).

firmed the estimated temperature and column density derived from the LTE modelling. Our initial assumption was that the detected *t*-HCOOH emission lines were optically thin and populated in an environment of LTE. The column density equation for optically thin molecular lines is expressed as (Goldsmith & Langer 1999):

$$N_u^{thin} = \frac{3g_u k_B}{8\pi^3 \nu S \mu^2} \int T_{mb} dV \quad (3)$$

In equation 3,  $g_u$  is the degeneracy,  $k_B$  is the Boltzmann constant,  $\mu$  is the electric dipole moment of the molecule,  $\nu$  is the rest frequency of the molecule,  $S$  is the strength

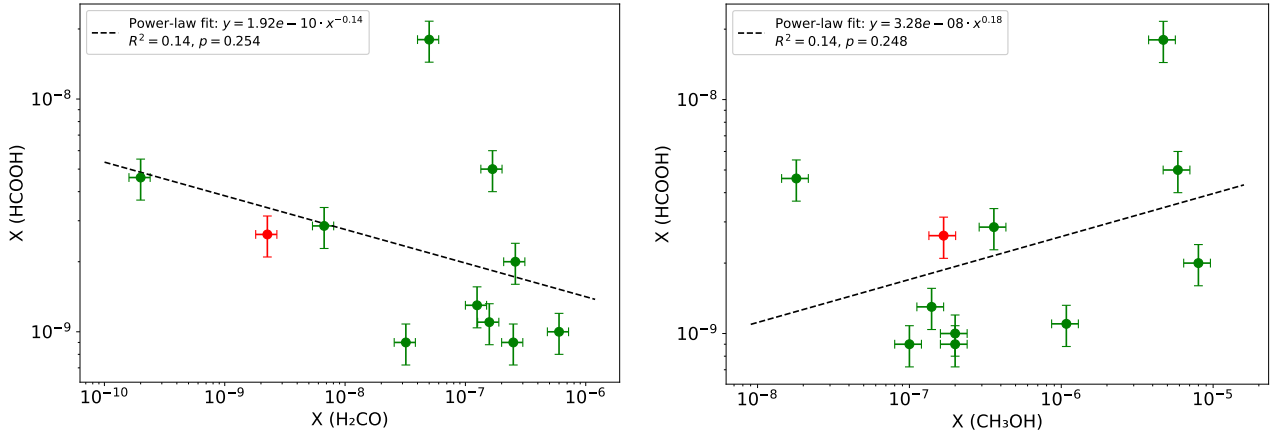


**Fig. 10** Relationship between the molecular abundances of HCOOH, CH<sub>3</sub>OH, and H<sub>2</sub>CO across different hot cores. The red data points correspond to measurements in G358.93–0.03 MM1, while the black dashed lines indicate the best-fit power-law.

**Table 5** Initial fractional abundances of H<sub>2</sub> and atomic elements at the start of the collapse phase.

Species	Abundance
H <sub>2</sub>	4.99×10 <sup>-1</sup>
H	2.00×10 <sup>-3</sup>
He	9.00×10 <sup>-2</sup>
N	7.50×10 <sup>-5</sup>
C	1.40×10 <sup>-4</sup>
O	3.20×10 <sup>-4</sup>
S	8.00×10 <sup>-8</sup>
Mg	7.00×10 <sup>-9</sup>
Na	2.00×10 <sup>-8</sup>
P	3.00×10 <sup>-9</sup>
Si	8.00×10 <sup>-9</sup>
Fe	3.00×10 <sup>-9</sup>
Cl	4.00×10 <sup>-9</sup>

of the molecule, and  $\int T_{mb} dV$  is the integrated intensity of the molecular line in km s<sup>-1</sup>. Under the LTE conditions, the total column density of the molecule is expressed as

$$\frac{N_u^{thin}}{g_u} = \frac{N_{total}}{Q(T_{rot})} \exp\left(\frac{-E_u}{k_B T_{rot}}\right) \quad (4)$$

In equation 4,  $T_{rot}$  represents the rotational temperature of the molecule, and  $Q(T_{rot})$  is the partition function at the estimated rotational temperature. The value of  $Q(T_{rot})$  of *t*-HCOOH are 8901.55 ( $T_{rot} = 300$  K), 5779.97 ( $T_{rot} = 225$  K), 3145.85 ( $T_{rot} = 150$  K), and 1112.92 ( $T_{rot} = 75$  K) (Müller et al. 2005). After rearranging, the equation 4 can be written as,

$$\ln\left(\frac{N_u^{thin}}{g_u}\right) = \ln(N) - \ln(Q) - \left(\frac{E_u}{k_B T_{rot}}\right) \quad (5)$$

Equation 5 showed that the  $E_u$  of the molecule and  $\ln(N_u/g_u)$  had a linear connection. Using equation 4, the value  $\ln(N_u/g_u)$  was estimated. Equation 5 suggests that the spectral parameters for different transition lines of *t*-HCOOH should be fitted with a straight line, where the slope is inversely proportional to the rotational temperature  $T_{rot}$ . After fitting a Gaussian model across the non-blended spectra of *t*-HCOOH, we determined the spectral line parameters of *t*-HCOOH for the rotational diagram. For fitting the equation 5 over the  $\ln(N_u/g_u)$  plotted against  $E_u$ , we used the MCMC approach using the Python module emcee (Foreman-Mackey et al. 2013). After fitting equation 5 using the MCMC method, the emcee module generates posterior probability distributions of  $N_T$  and  $T_{rot}$ . The rotational diagram and marginalized posterior probability distribution are shown in Figures 6 and 7. Based on the rotational diagram, we found the value of total column density ( $N_T$ ) and  $T_{rot}$  are  $(8.10 \pm 1.12) \times 10^{15}$  cm<sup>-2</sup> and 116.11 ± 7.62 K. We noticed that the values of  $T_{rot}$  and  $T_{ex}$  are nearly the same ( $T_{rot} \sim T_{ex}$ ), which indicates that *t*-HCOOH is in LTE conditions in G358.93–0.03 MM1.

### 3.2.3 Analysis of HCOOH towards G358.93–0.03 MM3

Using the LTE-modelled spectra, we also searched the emission lines of *t*-HCOOH and *c*-HCOOH towards G358.93–0.03 MM3, but we did not detect those molecules. The upper-limit column densities of *t*-HCOOH and *c*-HCOOH are  $\leq (2.53 \pm 0.62) \times 10^{13}$  cm<sup>-2</sup> and  $\leq (3.28 \pm 0.55) \times 10^{12}$  cm<sup>-2</sup>, respectively. The upper limits of their fractional abundance are  $\leq (7.23 \pm 2.32) \times 10^{-11}$  and  $\leq (9.37 \pm 2.45) \times 10^{-12}$ , respectively, where the value of  $N(H_2)$  towards G358.93–0.03 MM3 is  $(3.5 \pm 0.7) \times 10^{23}$  cm<sup>-2</sup> (Manna et al. 2024).

### 3.3 Spatial distributions of *t*-HCOOH

Using the CASA task IMMOMENTS, we generated the integrated emission maps of the detected *t*-HCOOH emission lines toward G358.93–0.03 MM1 (Figure 8). These maps are overlaid with the 291.31 GHz dust continuum to compare peak positions, which are found to be spatially coincident. The compact morphology suggests that *t*-HCOOH emission originates from the dense and warm inner region of hot core G358.93–0.03 MM1. We estimated the emitting region sizes ( $\theta_S$ ) by fitting 2D Gaussians with the IMFIT task, and the results are summarized in Table 4. The derived  $\theta_S$  values (0.40''–0.43'') are below than the synthesized beam sizes (0.43''  $\times$  0.36'' to 0.45''  $\times$  0.38''), indicating that the *t*-HCOOH emission is unresolved. Therefore, we do not draw any conclusions about the chemical morphology of *t*-HCOOH based on its spatial distribution. Thus, its spatial morphology remains uncertain and would benefit from higher-resolution observations.

## 4 DISCUSSIONS

### 4.1 Comparison and correlation analysis of HCOOH abundances with those in other sources

Here, we compared the derived abundances of HCOOH relative to H<sub>2</sub>, H<sub>2</sub>CO, and CH<sub>3</sub>OH between G358.93–0.03 MM1 and other sources. A comparison is made between the abundances of HCOOH found in G358.93–0.03 MM1 and various hot core and hot corino sources, such as NGC 6334 F (Nummelin et al. 1998; Zernickel et al. 2012), G327.3–0.6 (Nummelin et al. 1998; Wyrowski et al. 2006), G10.47+0.03 (Nummelin et al. 1998; Rolffs et al. 2011), G31.41+0.31 (García de la Concepción et al. 2022; Mininni et al. 2023; López-Gallifa et al. 2024), Sgr B2(N) (Belloche et al. 2013), Orion KL (Peng et al. 2019; Favre et al. 2015; Zernickel et al. 2012), W51 e1 (Liu et al. 2001; Rong et al. 2016), NGC 1333 IRAS 4A (Bottinelli et al. 2004; Maret et al. 2004; Quitoán-Lara et al. 2024), IRAS 16293–2422 B (Manigand et al. 2020; Persson et al. 2018), and NGC 6334 I (Zernickel et al. 2012). Figure 9 shows a bar diagram comparing the abundances of HCOOH towards G358.93–0.03 MM1 and other sources. It is evident that different hot cores and hot coronas have varying HCOOH abundances, which suggests that their chemical processes vary.

After comparison, we found the abundance of HCOOH relative to H<sub>2</sub> towards G358.93–0.03 MM1 is higher than most of the sources except for NGC 6334 I and NGC 1333 IRAS 4A. The abundance of HCOOH relative to H<sub>2</sub> towards G358.93–0.03 MM1 is comparable to that of G31.41+0.31 and slightly lower than that of W51 e1. Likewise, the HCOOH/CH<sub>3</sub>OH ratio for G358.93–0.03

MM1 is substantially higher than that of the majority of other sources, such as NGC 6334 F, G10.47+0.03, and W51 e1. The HCOOH/CH<sub>3</sub>OH ratio for G358.93–0.03 MM1 is significantly greater than that of G31.41+0.31 and Sgr B2 (N), suggesting that G358.93–0.03 MM1 has a particularly high HCOOH abundance relative to CH<sub>3</sub>OH. We observed that the NGC 1333 IRAS 4A exhibited the highest HCOOH/CH<sub>3</sub>OH ratio compared to all other sources, indicating that the region may produce more HCOOH because of various physical or chemical circumstances. The HCOOH/H<sub>2</sub>CO ratio towards G358.93–0.03 MM1 is remarkably high compared to most sources. The HCOOH/H<sub>2</sub>CO ratio towards G358.93–0.03 MM1 is significantly greater than those found in NGC 6334 F, G10.47+0.03, and G327.3–0.6. The only source with a much higher ratio is NGC 1333 IRAS 4A, whereas intermediate values are observed in W51 e1 and NGC 6334 I. The high HCOOH/H<sub>2</sub>CO ratio in G358.93–0.03 MM1 suggests that the formation pathway of HCOOH may be more efficient than H<sub>2</sub>CO, possibly due to variations in physical conditions such as temperature, density, or UV radiation exposure. Overall, these results indicate that G358.93–0.03 MM1 exhibits a relatively high abundance of HCOOH relative to H<sub>2</sub>, CH<sub>3</sub>OH, and H<sub>2</sub>CO, suggesting that this source is chemically rich in HCOOH relative to other interstellar environments. The enhanced HCOOH abundance may be linked to specific astrochemical pathways such as ice mantle processing, grain-surface reactions, or gas-phase chemistry influenced by shock activity or radiation fields. Further investigations of the physical conditions of G358.93–0.03 MM1 could provide insights into the dominant formation mechanisms of HCOOH in this region.

To explore the chemical relationship between HCOOH and its potential precursors, we examined the correlation between the observed abundances of HCOOH and two commonly proposed parent species, H<sub>2</sub>CO and CH<sub>3</sub>OH, across a sample of well-known hot cores. The resulting molecular correlations are presented in Figure 10.

In the first analysis (see left panel in Figure 10), we plotted the fractional abundance of HCOOH against that of H<sub>2</sub>CO and performed a linear regression to assess the strength and nature of their correlation. The power-law fitting yields a coefficient of determination ( $R^2$ ) of 0.14 and a *p*-value of 0.254. This result indicates a very weak and negative correlation between H<sub>2</sub>CO and HCOOH abundances, suggesting that the two molecules do not scale proportionally across different sources. From a chemical standpoint, this weak and negative correlation implies that while H<sub>2</sub>CO might participate in reaction pathways that produce HCOOH (e.g., through hydrogenation or radical chemistry on grain surfaces), its overall abundance is not a

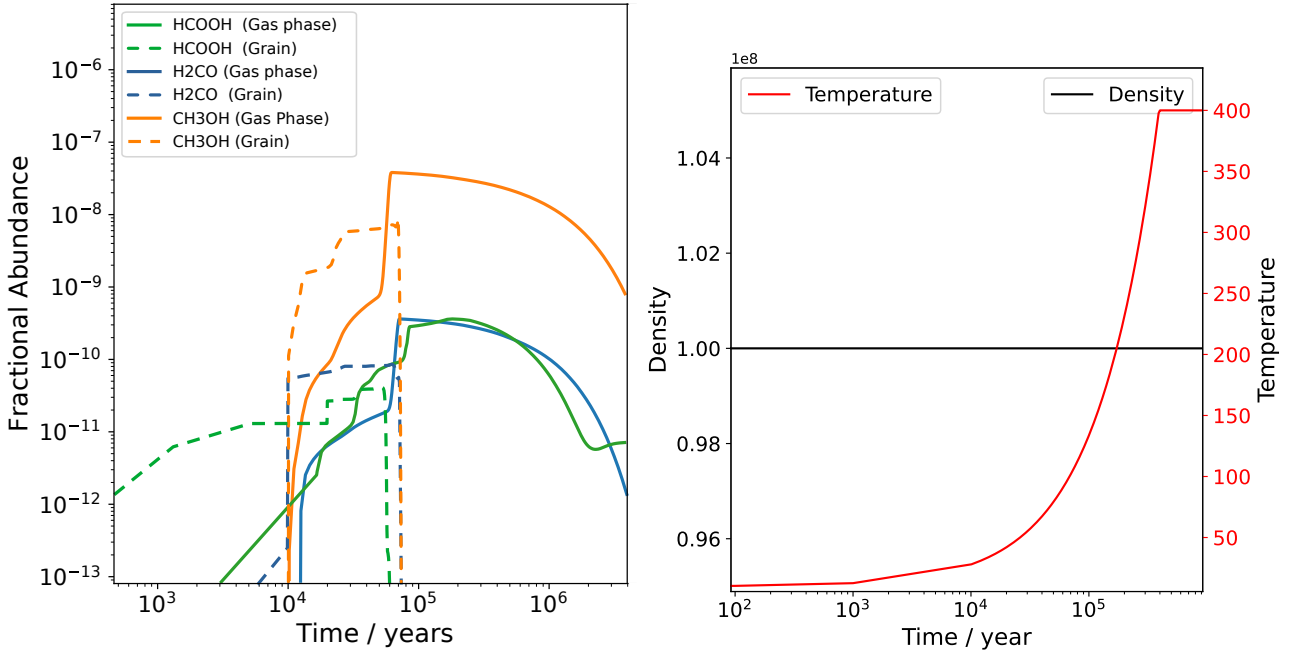


**Fig. 11** Time-dependent fractional abundances of HCOOH, H<sub>2</sub>CO, and CH<sub>3</sub>OH (left figure). Gas-phase species are represented by solid lines, while their grain (including both surface and mantle) counterparts are depicted with dashed lines of the same colour. The right-hand figure shows the temperature profile during the warm-up stage.

strong predictor of the amount of HCOOH present in these environments.

In the second analysis (see right panel in Figure 10), we examined the relationship between CH<sub>3</sub>OH and HCOOH abundances. Methanol is considered a more chemically relevant precursor to HCOOH, particularly through grain-surface chemistry. The regression between CH<sub>3</sub>OH and HCOOH yielded a positive slope of 0.18 and a *p*-value of 0.248, indicating a weak positive correlation. However, the *R*<sup>2</sup> value remained low at 0.14, which suggests significant scatter in the data. This weak positive correlation suggests that the chemical link between CH<sub>3</sub>OH and HCOOH might not be possible. This also indicates that the formation mechanism of HCOOH depends not only on the CH<sub>3</sub>OH but also on the other O-bearing molecules and local physical conditions that regulate grain-surface reaction networks and desorption mechanisms.

#### 4.2 Chemical modelling of HCOOH and other molecules

We computed a three-phase (gas + grain-surface + icy mantle) warm-up chemical model of HCOOH, CH<sub>3</sub>OH, and H<sub>2</sub>CO using the time-dependent gas-grain chemical code UCLCHEM (Viti 2013; Holdship et al. 2017) to investigate the modelled abundance and potential production mechanisms of these molecules. This chemical code

**Table 6** Peak fractional abundances and temperatures of HCOOH, CH<sub>3</sub>OH and H<sub>2</sub>CO predicted by the model under fast warm-up conditions.

Species	Phase	Temperature (K)	Abundance
HCOOH	Gas	127	$2.92 \times 10^{-9}$
	Surface	102	$1.26 \times 10^{-10}$
	Mantle	18	$3.81 \times 10^{-10}$
CH <sub>3</sub> OH	Gas	130	$2.82 \times 10^{-7}$
	Surface	110	$3.27 \times 10^{-8}$
	Mantle	10	$8.51 \times 10^{-8}$
H <sub>2</sub> CO	Gas	86	$3.21 \times 10^{-9}$
	Surface	55	$1.32 \times 10^{-10}$
	Mantle	10	$6.21 \times 10^{-10}$

investigates thermal and non-thermal desorption in both gas-phase and grain surface chemistry, considering various sources under different physical conditions in the ISM. This chemical code solves the rate of reactions to estimate the fractional abundances relative to hydrogen in the gas-phase and grain surface molecules in different environments where molecules exist (Viti 2013). In accordance with Garrod & Herbst (2006), we employed a two-stage physical model to explain the physical conditions in HMCs: free-fall collapse followed by a dynamically static warm-up. In the cold collapse stage (Phase I), the density of the gas ( $n_{H_2}$ ) increases from  $1 \times 10^2 \text{ cm}^{-3}$  to  $1 \times 10^8 \text{ cm}^{-3}$ , and the gas-grain temperature is fixed at 8 K. In chemical modelling, the cosmic ray ionization rate ( $\zeta$ ) and initial vi-

**Table 7** Comparison between peak gas-phase fractional abundances in the warm-up stage and the observed values.

Molecule	Modelled abundance	Modelled temperature (K)	Observed abundance	Excitation temperature (K)	Dominant reactions
CH <sub>3</sub> OH/H <sub>2</sub>	2.82×10 <sup>-7</sup>	130	(1.68±0.14)×10 <sup>-7</sup>	152±16	CH <sub>3</sub> O + H → CH <sub>3</sub> OH
H <sub>2</sub> CO/H <sub>2</sub>	3.21×10 <sup>-9</sup>	86	(2.26±0.19)×10 <sup>-9</sup>	90±6	HCO + H → H <sub>2</sub> CO
HCOOH/H <sub>2</sub>	2.92×10 <sup>-9</sup>	127	(2.62±0.29)×10 <sup>-9</sup>	120±15	HCO+OH → HCOOH
HCOOH/CH <sub>3</sub> OH	1.03×10 <sup>-2</sup>	–	(1.56±0.12)×10 <sup>-2</sup>	–	–
HCOOH/H <sub>2</sub> CO	0.91	–	(1.16±0.12)	–	–

sual extinction ( $A_V$ ) are  $1.3 \times 10^{-17} \text{ s}^{-1}$  and 2. During this period, the accretion rate of atoms and molecules on the grain surface is  $10^{-5} \text{ M}_\odot \text{ yr}^{-1}$ , and it depends on the gas density of the hot cores (Viti et al. 2004). We assumed the sticking probability during chemical modelling to be unity, meaning that all incoming hydrogen atoms will stick to the grain surface if they encounter an inactive site. The molecular species may hydrogenate or undergo rapid reactions with other species on the grain surface during this period. In the chemical model, the abundance of atoms relative to the solar values, which were used at the beginning of the collapse phase, is shown in Table 5, which is taken from Garrod (2013).

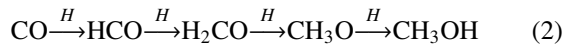
In phase II (warm-up stage), the temperature is increased from 8 K to 400 K, where  $n_{H_2}$  remains constant at  $1 \times 10^8 \text{ cm}^{-3}$ . We adopted the fast warm-up model with a timescale of  $7.12 \times 10^4 \text{ yr}$ , which was taken from Garrod (2013). Previous studies show that the fast warm-up model is well-suited to the physical conditions of high-mass star-forming regions (Suzuki et al. 2018). In this model, the warm-up phase lasts for  $7.12 \times 10^4 \text{ yr}$ , after which the temperature remains constant at its peak value of 400 K. In this stage, the temperature increases via the following expression (Garrod 2013).

$$T = T_0 + (T_{max} - T_0)(\Delta t/t_h)^n \quad (6)$$

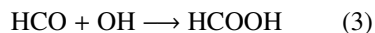
In Equation 6,  $T_0 = 8 \text{ K}$  represents the initial temperature at the start of the warm-up phase, and  $T_{max}$  denotes the maximum temperature reached at the end of the warm-up phase. The parameter  $\Delta t$  corresponds to the time duration of the warm-up phase, and  $t_h$  represents its characteristic timescale in the warm-up stage. The warm-up stage follows a first-order process, with  $n = 1$ . In this study, we set the fiducial values of  $t_h = 7.12 \times 10^4 \text{ yr}$  and  $T_{max} = 400 \text{ K}$ . During the warm-up phase, we also incorporated C-type shocks with a shock velocity of  $v_s = 20 \text{ km s}^{-1}$ , as adopted from Aota & Aikawa (2012) and Jiménez-Serra et al. (2018). The inclusion of C-type shocks is motivated by the observed outflow signatures in both H<sub>2</sub>CO and CH<sub>3</sub>OH. It is believed that the temperatures of the gas and dust are closely associated during the warm-up stage. The molecules no longer freeze during the warm-up phase, and both thermal and non-thermal desorption processes leave frozen molecules on the grain surface in the

gas-phase. Furthermore, we incorporated volcanic desorption, monomolecular desorption, grain mantle desorption, and co-desorption with H<sub>2</sub>O into our model (see Tables 1 and 2 of Viti et al. (2004)). This chemical model is similar to that of Garrod (2013), Manna & Pal (2024b), Manna & Pal (2024e), and Manna & Pal (2024f).

During chemical modelling, we used more than 300 reactions of HCCOH, CH<sub>3</sub>OH, and H<sub>2</sub>CO, which were taken from Garrod & Herbst (2006), Garrod et al. (2008), Garrod (2013), and the astrochemical databases of KIDA (Wakelam et al. 2012) and UMIST (McElroy et al. 2013). In the chemical model, the binding energies ( $E_D$ ) of HCOOH, CH<sub>3</sub>OH, and H<sub>2</sub>CO were 6000 K, 5000 K, and 4500 K, respectively. The  $E_D$  values of HCOOH, CH<sub>3</sub>OH, and H<sub>2</sub>CO were obtained from Suzuki et al. (2018). The behaviour of the fractional abundances relative to hydrogen of HCCOH, CH<sub>3</sub>OH, and H<sub>2</sub>CO over a time scale of  $7.12 \times 10^4 \text{ yr}$  is illustrated in Figure 11. Table 6 displays the peak abundances and the temperatures of the molecules. The formation of H<sub>2</sub>CO and CH<sub>3</sub>OH in the gas-phase is minimal; instead, it primarily occurs on dust grains through successive hydrogenation of CO accreted from the gas-phase. The dominant reaction of the formation pathway of H<sub>2</sub>CO and CH<sub>3</sub>OH on the dust grains is,



The high gas-phase abundance of CH<sub>3</sub>OH at low temperatures primarily results from chemical desorption from dust grains. In the simulation, a moderate increase in CH<sub>3</sub>OH abundance occurred around  $T \sim 40 \text{ K}$  because of the electronic recombination of HC(OH)OCH<sub>3</sub><sup>+</sup>, formed from the reaction between protonated methanol (CH<sub>3</sub>OH<sub>2</sub><sup>+</sup>) and H<sub>2</sub>CO when H<sub>2</sub>CO was abundantly released into the gas-phase. During simulation, we observed that the abundance of HCOOH in the gas-phase increased when H<sub>2</sub>O evaporated, thus improving the formation of OH through its reaction with atomic oxygen. The OH radical then reacted with HCO in the grain surface to produce HCOOH. The dominant reaction of the formation pathway of HCCOH on the grain surface is



At this stage, the grain surface synthesis of reaction 3 remains approximately ten times faster owing to the high HCO abundance. The final peak in the grain surface HCOOH abundance, along with the slight increase before the last gas-phase peak, is driven by enhanced gas-phase formation as OH desorbs from the dust grains. Eventually, surface-bound HCOOH evaporates, resulting in a peak gas-phase abundance of  $2.92 \times 10^{-9}$  relative to H<sub>2</sub>. Overall, grain surface reactions between HCO and OH are the primary pathway for HCOOH formation.

#### 4.3 Comparison between observed and modelled abundances of HCOOH

We compared the observed abundance of HCOOH with the modelled abundance derived from three-phase warm-up chemical modelling using UCLCHEM. This comparison aims to investigate the possible formation pathways of HCOOH towards G358.93–0.03 MM1. Physically, this comparison is suitable because the gas density of G358.93–0.03 MM1 is  $1.08 \times 10^8 \text{ cm}^{-3}$ , which is similar to the chemical model gas density. The comparison between the observed and modelled abundances is shown in Table 7. We found that the observed abundance of HCOOH relative to H<sub>2</sub> is nearly similar to the modelled value within a factor of 0.89. This indicates that HCOOH might be formed through the reaction between HCO and OH (Reaction 3) on the grain surface, which is further released in the gas-phase. We also found that the observed and modelled abundance of CH<sub>3</sub>OH and H<sub>2</sub>CO are nearly close, with the modelled values within the factors of 0.59 and 0.70, respectively. That indicates H<sub>2</sub>CO and CH<sub>3</sub>OH may be formed via the hydrogenation of CO on the grain surface (Reaction 2). The previous chemical model by Garrod & Herbst (2006) also indicates that reactions 2 and 3 are the dominant pathways for the formation of CH<sub>3</sub>OH, H<sub>2</sub>CO, and HCOOH on the grain surface. The observed and modelled abundance ratios of HCOOH/CH<sub>3</sub>OH and HCOOH/H<sub>2</sub>CO are in good agreement, differing by factors of only 1.51 and 1.27, respectively. Since the observed and modelled abundances, including temperatures, of three molecules are nearly close, this suggests that our chemical model is well-suited for the G358.93–0.03 MM1 hot core.

#### 5 SUMMARY AND CONCLUSION

In this article, we present the first detection of rotational emission lines of *t*-HCOOH towards hot core G358.93–0.03 MM1 using ALMA band 7. The column density and excitation temperature of *t*-HCOOH are  $(8.13 \pm 0.72) \times 10^{15} \text{ cm}^{-2}$  and  $120 \pm 15 \text{ K}$ , respectively. The fractional abundance of *t*-HCOOH relative to H<sub>2</sub> is  $(2.62 \pm 0.29) \times 10^{-9}$ . The column density ratios of *t*-HCOOH/CH<sub>3</sub>OH and *t*-

HCOOH/H<sub>2</sub>CO are  $(1.56 \pm 0.12) \times 10^{-2}$  and  $(1.16 \pm 0.12)$ , respectively. From the molecular correlation analysis, we find a negative correlation between HCOOH and H<sub>2</sub>CO, while HCOOH and CH<sub>3</sub>OH show a positive but statistically insignificant correlation. This suggests that H<sub>2</sub>CO and CH<sub>3</sub>OH may not serve as effective precursors of HCOOH. To understand the possible formation pathways of HCOOH and other molecules, we computed a three-phase warm-up chemical model using the gas-grain chemical code UCLCHEM. We found that the observed and modelled abundances of HCOOH are almost similar within a factor of 0.89. From these results, we claim that HCOOH might be formed through the reaction between HCO and OH on the grain surface, which is further released in the gas-phase. In addition to HCOOH, we also detected several other COMs, which we discuss in follow-up studies.

**Acknowledgements** We thank the anonymous reviewers for their helpful comments, which improved the manuscript. S.S. expresses gratitude to the Swami Vivekananda Merit-cum-Means Scholarship (SVMCM) for providing financial support for this research. This paper makes use of the following ALMA data: ADS/JAO.ALMA#2019.1.00768.S. ALMA is a partnership of ESO (representing its member states), NSF (USA), and NINS (Japan), together with NRC (Canada), MOST and ASIAA (Taiwan), and KASI (Republic of Korea), in cooperation with the Republic of Chile. The Joint ALMA Observatory is operated by ESO, AUI/NRAO, and NAOJ.

#### References

- Adams, F. C. 2010, *ARA&A*, 48, 47
- Aota, T., Aikawa, Y., 2012, *ApJ*, 761, 74
- Belloche, A., Müller, H. S. P., Menten, K. M., Schilke, P., Comito, C., 2013, *A&A*, 559, A47
- Beuther, H., Churchwell, E. B., McKee, C. F., & Tan, J. C. 2007, *Protostars and Planets V*, eds. B. Reipurth, D. Jewitt, & K. Keil (Tucson: University of Arizona Press), 165
- Bergwerf, H. 2015. MolView: an Attempt to Get the Cloud into Chemistry Classrooms. *ACS CHED CCCE News!* 2015, 19
- Biver, N., Bockelée-Morvan, D., Debout, V., Crovisier, J., Boissier, J., Lis, D. C., Dello Russo, N., et al., 2014, *A&A*, 566, L5
- Bottinelli, S., Ceccarelli, C., Lefloch, B., Williams, J. P., Castets, A., Caux, E., Cazaux, S., et al., 2004, *ApJ*, 615, 354
- Bouallagui, A., Zanchet, A., Mogren Al Mogren, M., Bañares, L., García-Vela, A., 2023, *ApJ*, 956, 22
- Brogan, C. L., Hunter, T. R., Towner, A. P. M., et al. 2019, *ApJL*, 881, L39

Beckwith, S. V. W., Sargent, A. I., 1991, *ApJ*, 381, 250

Comrie, A., Wang, K.-S., Hsu, S.-C., et al. 2021, CARTA: The Cube Analysis and Rendering Tool for Astronomy, v2.0.0, Zenodo, <https://doi.org/10.5281/zenodo.4905459>

Cao Q., Berski, S., Latajka, Z., Räsänen, M., Khriachtchev, L., 2014, *PCCP*, 16, 5993

Carpenter, J. M. 2000, *AJ*, 120, 3139

CASA Team, Bean, B., Bhatnagar, S., Castro, S., Donovan Meyer, J., Emonts, B., Garcia, E., et al., 2022, *PASP*, 134, 114501

Cazaux, S., Tielens, A. G. G. M., Ceccarelli, C., Castets, A., Wakelam, V., Caux, E., Parise, B., et al., 2003, *ApJL*, 593, L51

Chaabouni, H., Baouche, S., Diana, S., Minissale, M., 2020, *A&A*, 636, A4

Ehrenfreund, P., Charnley, S. B., 2000, *ARA&A*, 38, 427

Favre, C., Bergin, E. A., Neill, J. L., Crockett, N. R., Zhang, Q., Lis D. C., 2015, *ApJ*, 808, 155

Fontani, F., Pascucci, I., Caselli, P., et al. 2007, *A&A*, 470, 639

Foreman-Mackey, D., Hogg, D. W., Lang, D., Goodman, J., 2013, *PASP*, 125, 306

Furlan E., Fischer W. J., Ali B., Stutz A. M., Stanke T., Tobin J. J., Megeath S. T., et al., 2016, *ApJS*, 224, 5

García de la Concepción, J., Colzi, L., Jiménez-Serra, I., Molpeceres, G., Corchado, J. C., Rivilla, V. M., Martín-Pintado, J., et al., 2022, *A&A*, 658, A150

García de la Concepción, J., Jiménez-Serra, I., Corchado, J. C., Molpeceres, G., Martínez-Henares, A., Rivilla, V. M., Colzi, L., et al., 2023, *A&A*, 675, A109

Garrod, R. T., Herbst, E., 2006, *A&A*, 457, 927

Garrod, R. T., Widicus Weaver S. L., Herbst E., 2008, *ApJ*, 682, 283

Garrod, R. T., 2013, *ApJ*, 765, 60

Goldsmith P. F., Langer W. D., 1999, *ApJ*, 517, 209

Guélin, M., Cernicharo, J., 2022, *FrASS*, 9, 787567

Herbst, E., Garrod, R. T., 2022, *FrASS*, 8, 209

Hocking, W. H., 1976, *ZNatA*, 31, 1113

Holdship, J., Viti, S., Jiménez-Serra, I., Makrymallis, A., Priestley, F., 2017, *AJ*, 154, 38

Ikeda, M., Ohishi, M., Nummelin, A., Dickens, J. E., Bergman, P., Hjalmarson, Å., Irvine, W. M., 2001, *ApJ*, 560, 792

Irvine, W. M., Friberg, P., Kaifu, N., Matthews, H. E., Minh, Y. C., Ohishi, M., Ishikawa, S., 1990, *A&A*, 229, L9

Järvinen, T., Lundell, J. & Dopieralski, P., 2018, *Theor Chem Acc*, 137, 100

Jørgensen, J. K., Müller, H. S. P., Calcutt, H., Coutens, A., Drozdovskaya, M. N., Öberg, K. I., Persson, M. V., et al., 2018, *A&A*, 620, A170

Jørgensen, J. K., Belloche, A., Garrod, R. T., 2020, *ARA&A*, 58, 727

Jiménez-Serra, I., Viti, S., Quénard, D., Holdship, J., 2018, *ApJ*, 862, 128

Kobayashi, K., Ise, J.- ichi ., Aoki, R., Kinoshita, M., Naito, K., Udo, T., Kunwar, B., et al., 2023, *Life*, 13, 1103

Kurtz, S., Cesaroni, R., Churchwell, E., Hofner, P., & Walmsley, C. M. 2000, in *Protostars and Planets IV*, eds. V. Mannings, A. P. Boss, & S. S. Russell (Tucson: University of Arizona Press), 299

Lada, C. J., & Lada, E. A. 2003, *ARA&A*, 41, 57

Liu, S.-Y., Mehringer, D. M., Snyder, L. E., 2001, *ApJ*, 552, 654

Liu, S.-Y., Girart, J. M., Remijan, A., Snyder, L. E., 2002, *ApJ*, 576, 255

Liu, H.-L., Liu, T., Evans, N. J., Wang, K., Garay, G., Qin, S.-L., Li, S., et al., 2021, *MNRAS*, 505, 2801

López-Gallifa, Á., Rivilla, V. M., Beltrán, M. T., Colzi, L., Mininni, C., Sánchez-Monge, Á., Fontani, F., et al., 2024, *MNRAS*, 529, 3244

Manigand, S., Jørgensen, J. K., Calcutt, H., Müller, H. S. P., Ligterink, N. F. W., Coutens, A., Drozdovskaya, M. N., et al., 2020, *A&A*, 635, A48

Manna, A., Pal, S., 2023a, *JApA*, 44, 69

Manna, A., Pal, S., 2023b, *Ap&SS*, 368, 33

Manna A., Pal S., 2024a, *IJAsB*, 23, 14

Manna, A., Pal, S., 2024b, *ESC*, 8, 2401

Manna, A., Pal, S., 2024c, *RAA*, 24, 075014

Manna, A., Pal, S., 2024d, *NewA*, 109, 102199

Manna, A., Pal, S., 2024e, *ESC*, 8, 665

Manna, A., Pal, S., 2024f, *JApA*, 45, 3

Manna, A., Pal, S., Viti, S., Sinha, S., 2023, *MNRAS*, 525, 2229

Manna, A., Pal, S., Viti, S., 2024, *MNRAS*, 533, 1143

Manna, A., Pal, S., 2026, *NewA*, 122, 102465

Maret, S., Ceccarelli, C., Caux, E., Tielens, A. G. G. M., Jørgensen, J. K., van Dishoeck, E., Bacmann, A., et al., 2004, *A&A*, 416, 577

McElroy, D., Walsh, C., Markwick, A. J., Cordiner, M. A., Smith, K., Millar, T. J., 2013, *A&A*, 550, A36

McMullin, J. P., Waters, B., Schiebel, D., Young, W., & Golap, K. 2007, in Astronomical Society of the Pacific Conference Series, Vol. 376, Astronomical Data Analysis Software and Systems XVI, ed. R. A. Shaw, F. Hill, & D. J. Bell, 127

Mininni, C., Fontani, F., Sánchez-Monge, A., Rivilla, V. M., Beltrán, M. T., Zahorecz, S., Immer, K., et al., 2021, *A&A*, 653, A87

Mininni, C., Beltrán, M. T., Colzi, L., Rivilla, V. M., Fontani, F., Lorenzani, A., López-Gallifa, Á., et al., 2023, *A&A*, 677, A15

Müller, H. S. P., Schlöder, F., Stutzki, J., Winnewisser, G., 2005, *JMoSt*, 742, 215

Nummelin, A., Dickens, J. E., Bergman, P., Hjalmarson, A., Irvine, W. M., Ikeda, M., Ohishi, M., 1998, *A&A*, 337, 275

Ospina-Zamudio, J., Lefloch, B., Ceccarelli, C., Kahane, C., Favre, C., López-Sepulcre, A., Montarges, M., 2018, *A&A*, 618, A145

Peng, Y., Rivilla, V. M., Zhang, L., Ge, J. X., Zhou, B., 2019, *ApJ*, 871, 251

Perley, R. A., Butler, B. J., 2017, *ApJS*, 230, 7

Persson, M. V., Jørgensen, J. K., Müller, H. S. P., Coutens, A., van Dishoeck, E. F., Taquet, V., Calcutt, H., et al., 2018, *A&A*, 610, A54

Pickett, H. M., Poynter, R. L., Cohen, E. A., Delitsky, M. L., Pearson, J. C., Müller, H. S. P., 1998, *JQSRT*, 60, 883

Pinto, C. H., Vieira, I. S., Spada, R. F. K., 2025, *J. Mol. Model.*, 31, 21

Quitíán-Lara, H. M., Fantuzzi, F., Mason, N. J., Boechat-Roberty, H. M., 2024, *MNRAS*, 527, 10294

Robitaille, T. P., Whitney, B. A., Indebetouw, R., Wood, K., 2007, *ApJS*, 169, 328

Redondo, P., Largo, A., Barrientos, C., 2015, *A&A*, 579, A125

Reid, M. J., Menten, K. M., Brunthaler, A., et al. 2014, *ApJ*, 783, 130

Requena-Torres, M. A., Martín-Pintado, J., Rodríguez-Franco, A., Martín, S., Rodríguez-Fernández, N. J., de Vicente, P., 2006, *A&A*, 455, 971

Rivilla, V. M., Martín-Pintado, J., Jiménez-Serra, I., Rodríguez-Franco, A. 2013, *A&A*, 554, A48

Rivilla, V. M., Beltrán, M. T., Martín-Pintado, J., Fontani, F., Caselli, P., Cesaroni, R., 2017, *A&A*, 599, A26

Rodríguez-Almeida, L. F., Jiménez-Serra, I., Rivilla, V. M., Martín-Pintado, J., Zeng, S., Tercero, B., de Vicente, P., et al., 2021, *ApJL*, 912, L11

Rolffs, R., Schilke, P., Zhang, Q., Zapata, L., 2011, *A&A*, 536, A33

Rong, J., Qin, S.-L., Zapata, L. A., Wu, Y., Liu, T., Zhang, C., Peng, Y., et al., 2016, *MNRAS*, 455, 1428

Sanna, A., Cesaroni, R., Moscadelli, L., Zhang, Q., Menten, K. M., Molinari, S., Caratti o Garatti, A., et al., 2014, *A&A*, 565, A34

Suzuki, T., Majumdar, L., Ohishi, M., Saito, M., Hirota, T., Wakelam, V., 2018, *ApJ*, 863, 51

Suzuki T., Majumdar L., Goldsmith P. F., Tokuda K., Minamoto H., Ohishi M., Saito M., et al., 2023, *ApJ*, 954, 189

Tan, J. C., Kong, S., Butler, M. J., Caselli, P., & Fontani, F. 2013, *ASP Conf. Ser.*, 476, 123

Tan, J. C., Beltrán, M. T., Caselli, P., et al. 2014, in *Protostars and Planets VI* (Tucson: University of Arizona Press), 149

Vastel, C., Bottinelli, S., Caux, E., Glorian, J.-M., Boizot, M., 2015, *sf2a.conf*, 313

Viti, S., Collings, M. P., Dever, J. W., McCoustra, M. R. S., Williams, D. A., 2004, *MNRAS*, 354, 1141

Viti, S., 2013, *ascl.soft. ascl:1303.006*

Wakelam, V., Herbst, E., Loison, J.-C., Smith, I. W. M., Chandrasekaran, V., Pavone, B., Adams, N. G., et al., 2012, *ApJS*, 199, 21

Williams, D. A., Viti, S., 2014, *Observational Molecular Astronomy: Exploring the Universe Using Molecular Line Emissions*. Cambridge Univ. Press, Cambridge

Winnewisser, G., Churchwell, E., 1975, *ApJL*, 200, L33

Weingartner, J. C., Draine, B. T., 2001, *ApJ*, 548, 296

Wood, D. O. S., & Churchwell, E. 1989, *ApJS*, 69, 831

Wyrowski, F., Menten, K. M., Schilke, P., Thorwirth, S., Güsten, R., Bergman, P., 2006, *A&A*, 454, L91

Yamamoto, S. 2017, *Introduction to Astrochemistry: Chemical Evolution from Interstellar Clouds to Star and Planet Formation* (Berlin: Springer)

Zernickel, A., Schilke, P., Schmiedeke, A., Lis, D. C., Brogan, C. L., Ceccarelli, C., Comito, C., et al., 2012, *A&A*, 546, A87

Zuckerman, B., Ball, J. A., Gottlieb, C. A., 1971, *ApJL*, 163, L41

## APPENDIX

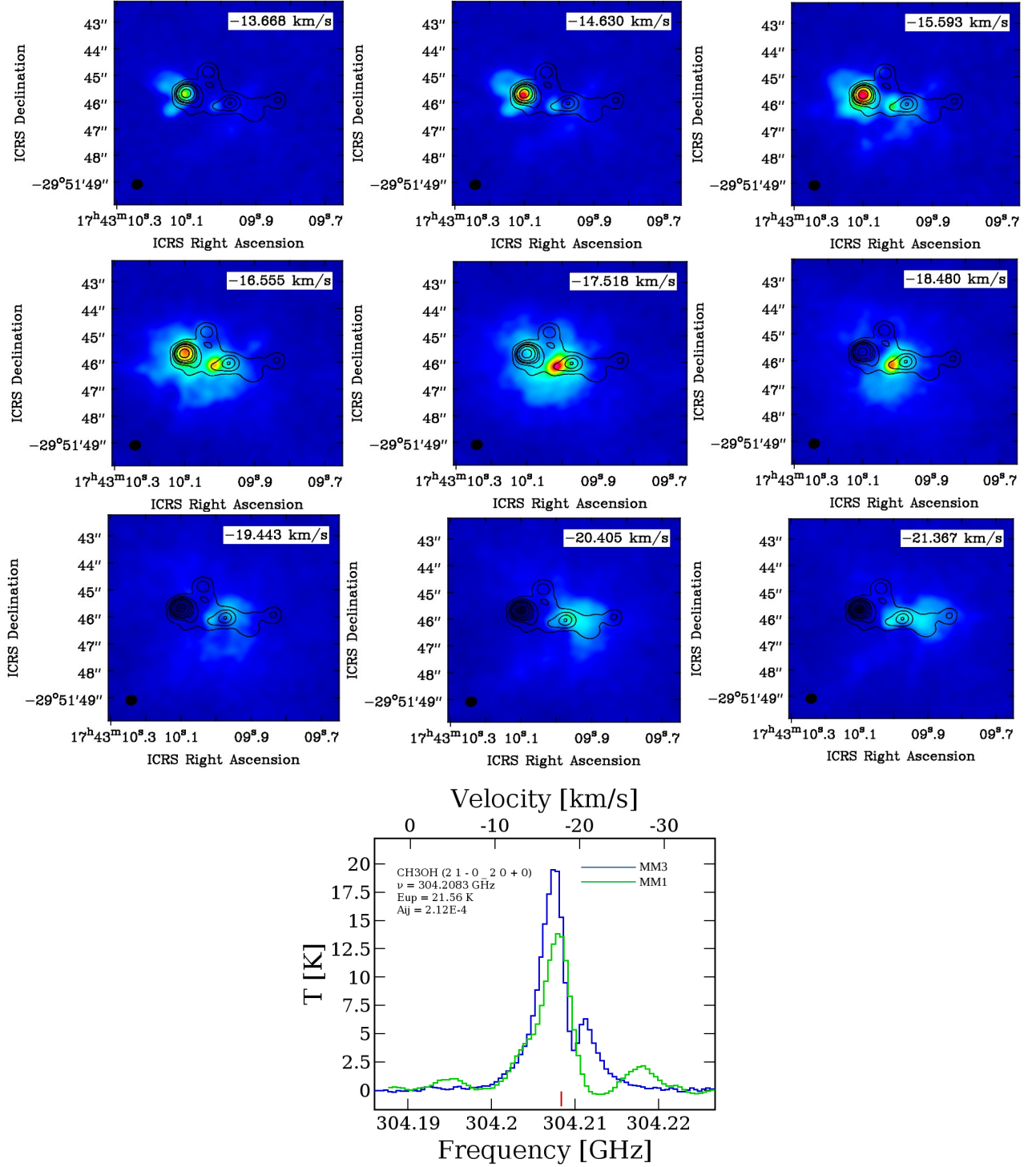


**Fig. A1** Channel maps of  $\text{CH}_3\text{OH}$  with the transition  $J = 2(1,-0)–2(0,+0)$  toward G358.93–0.03 are shown in the upper panel. The lower panel presents the corresponding emission spectra of  $\text{CH}_3\text{OH}$  ( $J = 2(1,-0)–2(0,+0)$ ) toward the G358.93–0.03 MM1 and MM3 cores.

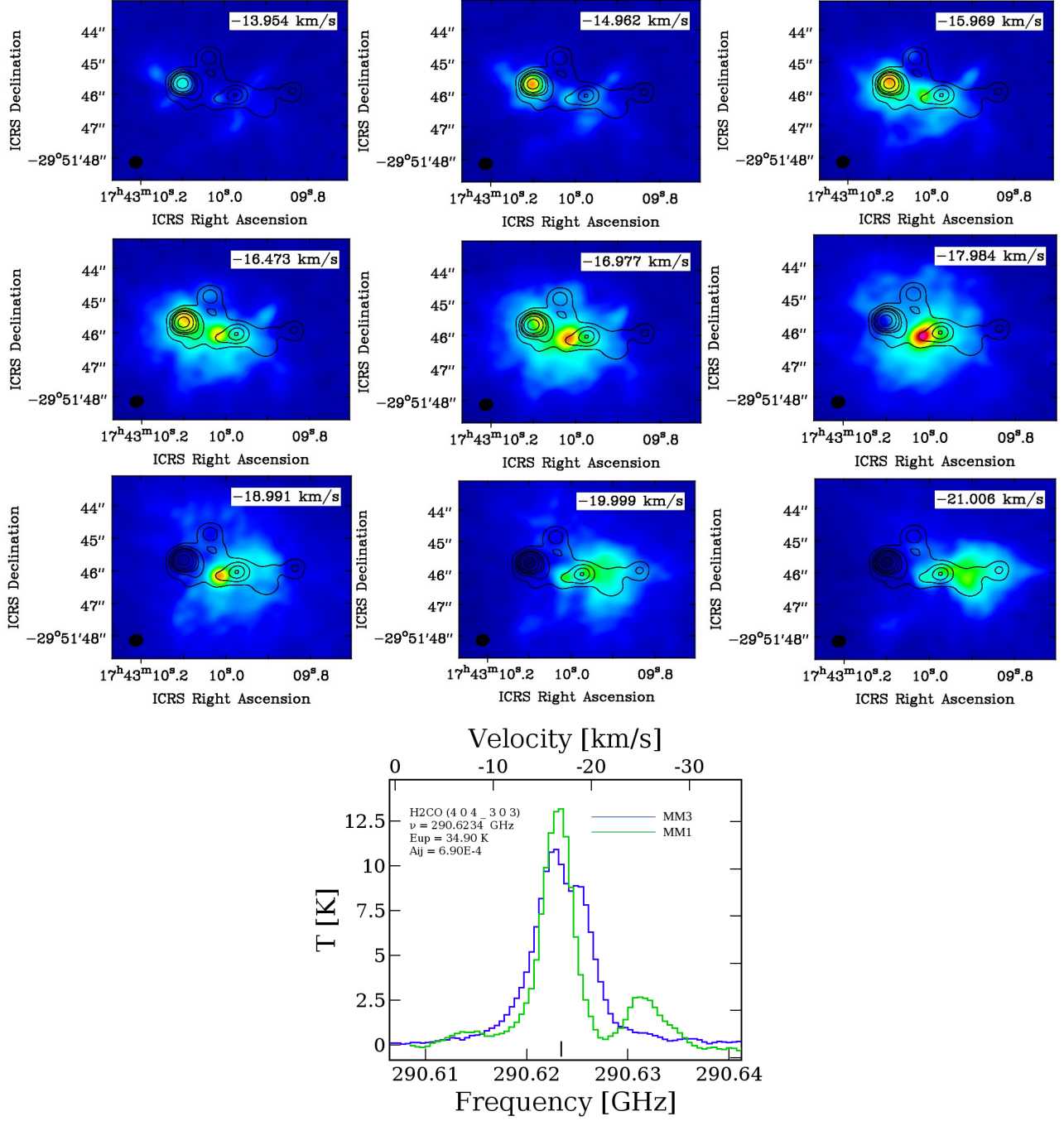


**Fig. A2** Channel maps of H<sub>2</sub>CO with the transition  $J = 4(0,4) - 3(0,3)$  toward G358.93–0.03 are shown in the upper panel. The lower panel presents the corresponding emission spectra of H<sub>2</sub>CO ( $J = 4(0,4) - 3(0,3)$ ) toward the G358.93–0.03 MM1 and MM3 cores.